Dual effects of *ARX* poly-alanine mutations in human cortical and interneuron development

AUTHORS:

Vanesa Nieto-Estevez[1,2], Parul Varma[1,2], Sara Mirsadeghi[1,2], Jimena Caballero[1,2], Sergio Gamero-Alameda[1,2], Ali Hosseini[3], Sonal Goswami[1,2], Marc J. Silvosa[4], Drew M. Thodeson[5], Zane R. Lybrand[1,2,4], Michele Giugliano[3], Christopher Navara[1,2,6] and Jenny Hsieh[1,2 #]

AFFILIATIONS:

1. Department of Neuroscience, Developmental and Regenerative Biology, The University of Texas at San Antonio, San Antonio, TX, USA
2. Brain Health Consortium, The University of Texas at San Antonio, San Antonio, TX, USA
3. Neuroscience Area, International School of Advanced Studies, Trieste, Italy
4. Division of Biology, Texas Woman's University, Denton, TX, USA.
5. Departments of Pediatrics and Neurology and Neurotherapeutics, Division of Child Neurology, UT Southwestern Medical Center, Dallas, TX 75390, USA
6. Stem Cell Core, The University of Texas at San Antonio, San Antonio, TX, USA

[#]CORRESPONDING AUTHOR: Jenny Hsieh, PhD; Email: Jenny.Hsieh@utsa.edu

Key words

ARX, epilepsy, brain development, interneuron migration, poly-alanine expansion, organoids

Summary

Mutations in *ARX*, an X-linked gene, are implicated in a wide spectrum of neurological disorders including patients who have intellectual disability and epilepsy. Mouse models have shown that Arx is critical for cortical development and interneuron migration, however they do not recapitulate the full phenotype observed in patients. Moreover, the epilepsy in many patients with poly-alanine tract expansion (PAE) mutations in *ARX* show pharmacoresistance, emphasizing the need to develop new treatments. Here, we used human neural organoid models to study the consequences of PAE mutations, one of the most prevalent mutations in *ARX*. We found that PAE mutations result in an early increase in radial glia cells and intermediate progenitor cells, and premature differentiation leading to a loss of cortical neurons at later timepoints. Moreover, *ARX* expression is upregulated in CO derived from patient at 30 DIV which alters the expression of *CDKN1C*, *SFRP1*, *DLK1* and *FABP7*, among others. We also found a cell autonomously enhanced interneuron migration, which can be rescued by CXCR4 inhibition. Furthermore, ARX^{PAE} assembloids had hyper-activity and synchrony evident from the early stages. These data provide novel insights to the pathogenesis of these and likely related human neurological disorders and identifies a critical window for therapeutic interventions.

Introduction

The Aristaless-related homeobox (*ARX*) gene is a paired-like homeodomain (HD)-containing transcription factor located on the X-chromosome that can function as either an activator or a repressor [1-4]. In addition to the HD, ARX contains: a conserved aristaless domain, an octapeptide domain, three nuclear localization sequences, a central acidic domain and four poly-alanine tracts [4]. Mutations in *ARX* are associated with a broad spectrum of phenotypes that can be divided into two groups: (1) mutations in the HD and mutations which produce truncated proteins resulting in severe intellectual disabilities (ID), autism spectrum disorder (ASD), seizures, and brain malformations, notably lissencephaly and agenesis of the corpus callosum [5-7], and (2) missense mutations and in-frame expansions of the first two poly-alanine tracts that are associated with ID, ASD, and epilepsy but no structural brain malformations [6,8,9]. Disease-causing poly-alanine expansion (PAE) mutations have been identified in nine genes, and eight of them (including *ARX*) encode transcription factors [10,11]. Unlike the more common and well-studied poly-glutamine repeats, PAEs are shorter, often less than 20 alanines, and result in developmental disorders, similar to those seen with PAE mutations in ARX, suggesting a similar molecular/genetic mechanisms underlying PAE-related disorders [10,11].

During development, *Arx* is expressed in the nervous system, pancreas and testis. In adult mice, it has been found in brain, muscle, heart, and liver [12,13]. In the brain, it is expressed in both cortical progenitor cells as well as postmitotic cortical ɣ-aminobutyric acid-containing (GABAergic) interneurons, and has been shown to play critical roles during interneuron migration and cortical development [12,14,15]. Studies using knock-out (KO) mouse models or mutations in the HD of *Arx* have recapitulated the phenotype of patients with the most severe cases of ARX-associated epilepsy. Although these mice show aberrant tangential migration and reduced GABAergic interneurons in the cortex and other brain regions [16,17], perinatal lethality has prevented any further analysis in adolescent or adult mice [13]. To overcome this limitation, conditional KO mice, lacking *Arx* expression selectively in interneuron progenitor cells was used, and showed a similar loss of interneurons [18-20] and these mice developed seizures [18]. Moreover, loss of *Arx* in cortical projection neuron progenitor cells resulted in a proliferation defect and decreased the number of upper-layer cortical neurons [14,15,21]. Interestingly, mice lacking *Arx* in cortical projection neuron precursors did not develop seizures, despite being hyperactive and having behavioral abnormalities [22]. In contrast, mice with a PAE mutation knocked in showed fewer GABAergic interneurons in the cortex [17,23] and had seizures [24-27]. Although these mouse models have advanced our understanding the role ARX plays in several neurological conditions, they fail to fully recapitulate its complete role in human brain

development as mice miss key aspects of human development. This is particularly obvious when mouse models are used to develop new therapies; unfortunately effective drugs in animals frequently fail in clinical trials [28]. Moreover, epilepsy in many patients with *ARX* mutations are resistant to existing pharmaceutical treatments. Thus, there is a clear need for new models for studying neurological diseases and drug screening.

Postmortem tissues from patient with these rare neurological diseases are not often available for study, especially from pediatric patients. Neural organoids can serve as excellent *in vitro* models for studying human development because they mimic key aspects of human brain development, such as presence of outer radial glial cells (oRGCs), expansion of cortical layers and interneuron migration [29-33], and importantly opens up opportunities to develop new treatments for human neurological disorders [34-36].

To study the role of *ARX* PAE mutations in human brain development and epilepsy, we recruited three male patients with a PAE in the second tract of *ARX*, plus three healthy male controls. We focused on male patients because *ARX* is located on the X Chromosome, and females present with a milder and more variable phenotypes[18]. We then generated two types of human regionalized neural organoids from human induced pluripotent stem cells (hiPSCs), cortical and ganglionic eminences organoids (henceforth referred as CO and GEO, respectively; previously known as human cortical spheroids, hCS, and human subpallium spheroids, hSS) [30,33,37]. COs present a cytoarchitecture that resembles the cortical plate during development with progenitor cells located around ventricular-zone-like structures, and cortical neurons are differentiated in an inside-out manner [33,38]. GEOs contain ventral progenitor cells similar to interneuron progenitor cells in ganglionic eminences (GE) that migrate to the cortex and integrate into the cortical network [30,38,39]. We used immunohistochemistry and single-cell RNA sequencing (scRNA-seq) at different developmental timepoints in patient-derived CO and GEO, to test the hypothesis, based on animal studies [12,14,15], that *ARX* PAE mutations would result in cortical and interneuron defects.

Our results revealed that ARX is upregulated in CO derived from patients, compared to healthy controls at 30 days *in vitro* (DIV). We also observed an increase in radial glial cells (RGCs) and intermediate progenitor cells in patient-derived CO at 30 DIV. Gene-expression analysis of these RGCs revealed that they either maintain or increase the expression of genes such as *NESTIN* and *HES5*, but downregulate *HES1, PAX6* and *DLK1*, leading to a premature neuronal differentiation, as shown by the increased expression of *TUBB3*. Moreover, patient-derived CO at 30 DIV showed a decreased expression of *CDKN1C*, cyclin dependent kinase inhibitor 1C, which negatively regulates cellular proliferation. This activation of RGCs in turn would have led to increased cortical neurogenesis that initially exhausts the RGC population,

and eventually results in decreased cortical neurons later in development, as evidenced by the reduced expression of cortical neuron markers such as *CTIP2* and *SATB2* at 120 DIV. We also found that PAE decreased the number of ARX$^+$ cells and GABAergic neurons in GEO and accelerated the migration of interneurons in the cortex, probably due to overexpression of CXCR4/CXCL12. Interestingly, CXCR4 inhibition is sufficient to reduce interneuron migration to control level. These cellular abnormalities can alter neuronal circuitry and lead to a hyper-active and more synchronized activity. These results demonstrate a dual role of ARX during human brain development, and distinct consequences of the PAE mutation in cortical progenitor cells and interneurons. These findings are consistent with the phenotype described in patients and mouse models, and provide critical information about the pathology of human PAE mutations for developing new treatments for neurological disorders.

Results

Generation and characterization of CO and GEO

ARX is a key transcription factor expressed during brain development that controls cortical progenitor cell differentiation as well as interneuron migration in animal models [12,14,15]. Although most of what is known about ARX function comes from mouse models, it is unclear if these models fully recapitulate its role during human brain development, thus necessitating the need for human models to study. To address this challenge, we turned to CO and GEO *in vitro* models of human brain development [30,33,39] to elucidate the role(s) ARX plays in human brain development and in the pathogenesis of epilepsy. To confirm our organoids accurately reproduced the sequence of development observed by others, we used immunostaining and scRNA-seq. Neural differentiation was achieved through SMAD inhibition to generate COs from hiPSCs [33] (Fig. S1A). We observed that after 30 DIV, COs had ventricle-like structures, defined by PAX6$^+$ (Paired Box 6) cells [expressed in dorsal cortical progenitor cells [40]], surrounded by maturing neurons [labeled with CTIP2, expressed in deep-layer cortical neurons [41-43]] (Fig. S1B). To further study various cell types in COs at 30 DIV, we performed scRNA-seq analysis and found that, in addition to containing RGCs and deep-layer neurons, these organoids also include cycling and intermediate progenitor cells, a population of early Cajal-Retzius cells, and a small percentage of interneurons (Fig. S1C). Similar analysis of CO at 120 DIV revealed the presence of oRGCs marked by expression of *FAM107A* (family with sequence similarity 107 member A) and *HOPX*, key factors expressed in human oRGCs [44,45]. We also observed CTIP2$^+$ and SATB2$^+$ cortical neurons in COs at 120 DIV (Fig. S1D-E). While CTIP2 labeled deep-layer neurons, SATB2 is expressed in upper-layer neurons [42,46]. We also generated GEOs resembling the GE by modulating WNT (Wingless-related integration site) and SHH (Sonic Hedgehog) pathways

through addition of IWP-2 and SAG (Smoothened receptor agonist) [30]. We found that GEO at 30 DIV contained KI67$^+$ and NKX2.1$^+$ cells (Fig. S1F-G). KI67 labels proliferative cells in the G1, S, G2, and M phases [47], while *NKX2.1* is expressed in progenitor cells in the medial GE and in the preoptic area [48,49]. Our analysis of GEO at 120 DIV, a later developmental timepoint, revealed TUJ1$^+$, GABA$^+$ and CXCR4$^+$ neurons. (Fig. S1H-I). CXCR4 (C-X-C motif chemokine receptor 4) has been shown to play an important role in interneuron migration [50-52]. The specific set of genes expressed by each cluster/cell type identified by scRNA-seq in CO and GEO at 30 and 120 DIV are shown in Fig. S2. and supplementary data tables. These results demonstrate the feasibility of growing neural organoids resembling cortical and subpallium regions of human brain as described previously [30,33,38].

Expression of ARX and impact of PAE in CO and GEO

We first interrogated our scRNA-seq dataset and found that ARX is expressed in control COs and GEOs at 30 and 120 DIV (Fig. 1A-B). As predicted, a higher percentage of *ARX*-expressing cells was found in GEO when compared to CO. Furthermore, and consistent with known data, for those cells expressing *ARX* in CO, a high percentage where proliferative at the earlier time point (Fig. 1A) [12]. We also observed progenitor cells and cortical neurons expressing *ARX* in COs at both timepoints. In GEO, *ARX* was expressed in both progenitor cells and GABAergic neurons (Fig. 1B). These data were consistent with the expression of *ARX* in human brain tissue (Fig. 1C). Thus, during embryonic development, *ARX* expression is higher in the GE/striatum than in the cortex, similar to data from mice [12]. Furthermore, *ARX*-expressing cells can be found both in the cortex and the striatum throughout adult life, although the level of expression is lower than in embryonic tissues.

To study the role of ARX during human development, we recruited three healthy controls and three patients with eight additional alanines in the second poly-alanine tract of ARX (Table 1). Six lines of hiPSCs were generated (one per person) and two clones per line were used in all experiments (or as otherwise indicated). All the lines expressed pluripotency markers (NANOG, SOX2, OCT4, LIN28, SSEA-4 and TRA-1-6), lost reprogramming factors (as shown by the lack of expression of the vectors used for reprograming) and maintained normal karyotype throughout the study (Fig. S3). The number of alanines was confirmed by PCR amplification followed by Sanger sequencing (data not shown). Then we first assayed ARX expression in COs and GEOs derived from patients (Fig. 1D-G). We found a significant increase in ARX expression among cells in ARX^{PAE} COs at 30 DIV when compared to controls (P=0.0177, d=0.944, n=13-14; Fig. 1D-E). scRNA-seq analysis confirmed this increase in *ARX* expression COs (Fig. S4) and it was consistent in the three lines (Fig. S5). No differences were found at 60 or 120 DIV COs (data not shown). In contrast,

ARX^{+} cells decreased in ARX^{PAE} GEOs at 30 and 60 DIV (30 DIV: P= 0.0033, d=-1.367, n=14-15; 60 DIV: P=0.0001, d=-1.823, n=16; Fig. 1F-G and Fig. S9), and we did not see any significant difference at 120 DIV (data not shown). Although it has been reported that PAE produces nuclear inclusions and/or cytoplasmatic localization [26,53-55], ARX was restricted to the nucleus without forming inclusions in COs and GEOs. Our data demonstrated that ARX is expressed in cortical and subpallium tissues and that PAE affects *ARX* expression differently in COs and GEOs.

PAE affects cortical development

The expression of ARX in progenitor cells in COs at 30 DIV and the increased expression of *ARX* in ARX^{PAE} COs prompted us to investigate how PAE affects cortical development. We first analyzed the size of control and ARX^{PAE} COs over time. We found that ARX^{PAE} COs were larger than control COs at 14 and 21 DIV (Fig. S6A-B, 14DIV: P= 0.0005, 21DIV: P= 0.0226, 60DIV: P= 0.3557). Interestingly, one of the patients used in the study presented a head circumference of 61 cm at 18-year-old which is 99.99% percentile (Z score of 4.07). To explore whether the increased size was due to an increase in proliferation, we labeled dividing cells by immunostaining against KI67 in sections from control and ARX^{PAE} COs at 30 DIV [47]. We found a trend towards more KI67^{+} cells in ARX^{PAE} COs (P=0.064, d=0.782, n=12-13; Fig. 2A-B). To investigate whether PAE affects cortical progenitor cells, we examined the expression of PAX6, HES1 and HES5 (hes family bHLH transcription factor 1 and 5), well-known markers of progenitor cells [40,56,57]. ARX^{PAE} COs had fewer PAX6^{+} cells than controls (P=0.0089, d=0.955, n=17; Fig. 2A-B). Based on RNAscope analyses, cellular *HES1* expression was reduced whereas *HES5* was increased in ARX^{PAE} COs (Fig. 2C-D; *HES1*: P=0.0415, d=-1.054, n=11-15; *HES5*; P=0.0465, d=0.707, n=9-15). scRNA-seq analysis showed similar trends in *PAX6*, *HES1* and *HES5* (Fig. S4 and Fig.S5). We then analyzed the expression of *TBR2*, a marker of intermediate progenitor cells[58,59]; and we found a significant increase of *TBR2* expression in ARX^{PAE} COs compared to controls (Fig. 2E, P=0.0077, n=12-17). To obtain a more comprehensive profile of the cell composition within the control and ARX^{PAE} COs, we performed cell-type proportion analysis using the scRNA-seq dataset and observed a significant increase in the percentage of RGCs in ARX^{PAE} COs (P=0.04; Fig. 2F). It has been shown Arx regulates the expansion of cortical progenitor cells in mouse through repression of Cdkn1c which negatively inhibit cell proliferation [14]. Thus, we then analyzed the expression of *ARX*, *CDKN1CA*, *CDKN1B* and*CDKN1C* in control and ARX^{PAE} COs at 30 DIV by RT-qPCR (Fig. 2G). While *ARX* expression was increased in ARX^{PAE} COs, as it was also found by IHC and scRNA-seq, *CDKN1C* levels were decreased (Fig. 2G; *ARX*: P=0.0008, n=12-18; *CDKN1C*; P=0.0195, n=12-17). This data is consistent

with previous findings in mouse, and it could explain the increased number of RGCs and intermediate progenitor cells observed in COs derived from patients.

To further investigate the effect of PAE on progenitor cells, we subclustered the RGCs and obtained 9 subclusters (Fig. 3A). *ARX* was mostly expressed in subclusters 1, 2 and 3; and was increased in ARX^{PAE} COs (Fig. 3B). *NESTIN* and *HES5* were highly expressed in all 9 subclusters, and their higher expression was observed in ARX^{PAE} COs; however, we found *HES1* and *PAX6* were decreased. *DLK1* (delta like non-canonical Notch ligand 1)—a non-canonical ligand of Notch that inhibits its function and has been found to be expressed in a subpopulation of human cortical progenitor cells [60,61]— was also abundantly expressed in some subclusters in ARX^{PAE} COs, compared to only a few cells in controls. Interestingly, *DLK1* has also been shown to promote neural differentiation, we indeed observed an increase in *TUBB3* (tubulin beta 3 class III, a pan neuronal marker) expression in ARX^{PAE} COs. In addition, at 30 DIV we found 3196 differentially expressed genes in RGCs in ARX^{PAE} COs, out of which 2642 were upregulated and 554 were downregulated (Fig. 3C). Among the upregulated genes, we found *NESTIN*, *FABP7*, *DLK1* and *SFRP1* ($p<0.05$ & $logFC>1$; Fig. 3C and Fig. S4). While *NESTIN*, *FABP7* and *DLK1* are canonical markers of RGCs, SFRP1 (secreted frizzled related protein 1) has been shown to inhibit WNT signaling. Studies have also suggested that upregulation of *SFRP1* represses *PAX6* [62-64]. Together, these data suggested that *ARX* increase due to PAE produces an expansion of RGCs and intermediate progenitor cells in COs, which may undergo a premature differentiation by downregulating genes like *PAX6, HES1* and *CDKN1C,* and upregulating genes such as *NESTIN*, *HES5*, *TUBB3*, *DLK1* and *SFRP1*.

Next, we investigated the long-term consequences of PAE in the cortex by analyzing 120 DIV COs (Fig. 4). We observed a significant decrease of $NEUROD1^+$ neuronal progenitor cells (P=0.0426, d=-0.772, n=16) and $CTIP2^+$ deep-layer neurons (P=0.0294, d=-0.828, n=15-16) in ARX^{PAE} CO at 120 DIV (Fig. 4A-). We also found a trend towards fewer $PAX6^+$ cells (P=0.2502, d=-0.472, n=12-13) and $SATB2^+$ upper-layer neurons (P=0.0829, d=-0.701, n=14; Fig. 4A-B). We saw no difference in the percentage of VIM^+ RGCs (P=0.5488, d=0.214, n=15-17), but we found a significant reduction in $FAM107A^+$ oRGCs (P=0.0086, d=-1.052, n=12-15; Fig. 4C-D). Cell-type proportion analyses in scRNA-seq data at 120 DIV also showed a trend towards a decrease in deep-layer neurons (Fig. 4E B and Fig. S7 and S8). Taken together, our data show that expansion in the second poly-alanine track leads to an increase of *ARX* in COs, which promotes the expansion of RGCs and their premature differentiation, resulting in an overall reduction in mature cortical neurons.

PAE alters interneuron differentiation and migration

As we found higher ARX expression in GEOs than in COs, we next studied the effect of PAE in GEO at different timepoints (Fig. 5). We first analyzed the size of control and ARX^{PAE} GEOs over time and found that ARX^{PAE} GEOs were larger than controls at all time points and these size differences were more prominent than in COs (Fig. S6 C-D, 14DIV: P= 0.0084, 21DIV: P= 0.0004, 60DIV: P= 0.0059). We next examined the expression of KI67 and NKX2.1, and observed a trend towards fewer $KI67^+$ proliferative cells in ARX^{PAE} GEOs at 30 DIV, but no change in NKX2.1 (KI67: P= 0.069, d=-0.672, n=14-18; NKX2.1: P=0.55, d=-0.218, n=14-17; Fig. 5A-B). Similarly, cell type proportion analysis in scRNA-seq data also revealed a trend towards fewer intermediate progenitor cells (Fig. 5C). At 120 DIV, ARX^{PAE} GEOs had fewer $TUJ1^+$ and $GABA^+$ neurons (TUJ1: P= 0.0154, d=-1.196, n=8-13; GABA: P=0.0641, d=-0.85, n=9-13; Fig. 5D-E). Similar reduction in interneurons was found by scRNA-seq as well (Fig. 5F and Fig.S9 and Fig. S10). We also found an increase in CXCR4 in ARX^{PAE} GEOs (P= 0.0037, d=1.313, n=10-13; Fig. 5D-E). CXCR4 and its ligand CXCL12 are important for neuronal migration [65]. Interestingly, we also detected a higher expression of CXCL12 in ARX^{PAE} COs at 120 DIV by scRNA-seq (Fig. S7 and Fig. S8). These data suggest PAE affects interneuron differentiation.

During development, interneurons are formed in the GE and migrate along circuitous routes to the cortex to integrate with projection neurons and form the cortical neuronal circuits [49,66]. Organoid models can recapitulate interneuron migration by fusing one GEO and one CO (referred as assembloids). We labeled interneuron progenitor cells in GEOs at 50 DIV using a DLX1/2b GFP-expressing lentivirus (Fig. 6A, Experimental Design 1). DLX1 and DLX2 are expressed in ventral progenitor cells and promote interneuron differentiation and migration [49,67]. We also labeled COs using an AAV-synapsin-mCherry virus; these $mCherry^+$ cells did not migrate into GEOs (Fig. S11AC). After 10 DIV, one GEO was placed in close contact with one CO to allow their fusion and the migration of the DLX1/2-GFP^+ cells from the GEO to the CO. Migration into the CO was assayed at 30 days after fusion by time-lapse imaging. We observed a similar percentage of cells moving in ARX^{PAE} assembloids (condition 2) compared to controls (condition 1, Fig. S12D). However, DLX1/2-GFP^+ cells migrated further and faster in ARX^{PAE} assembloids (Distance: P= 0.0110, d=0.607, n=38-48; Velocity: P= 0.0090, d=0.624, n=38-47; Fig. 6B-D, Fig. S12 and videos 1-4). Moreover, in control assembloids most of the cells migrated less than 300 µm, whereas a higher percentage of cells migrated more than 300 µm in ARX^{PAE} assembloids (Fig. S12C). To investigate if the faster migration of interneurons leads to an increase of neurons in the cortex, we quantified the GFP^+ area in the CO and GEO side of the assembloids, and both ARX^{PAE} and control assembloids showed similar

percentages of GFP$^+$ area (Fig. S11C). To determine whether the accelerated migration observed in ARX^{PAE} assembloids was due to a cell-autonomous effect, we fused ARX^{PAE} GEOs to control COs (condition 3) to create inter-individual assembloids, where interneurons would have PAE and the cortical side would express wild-type ARX (Fig. 6C-D). We found DLX1/2-GFP$^+$ cells migrated a similar distance and had a similar velocity than ARX^{PAE} assembloids (Distance: P= 0.0125, d=0.522, n=48; Velocity: P= 0.0081, d=0.53, n=47-48). To test whether the defects observed in COs were sufficient to affect interneuron migration, we fused control GEOs to ARX^{PAE} COs (condition 4). Interneurons in this condition migrated at a similar velocity and similar distance to control assembloids (Distance: P= 0.0370, d=-0.52, n=30-38; Velocity: P= 0.0423, d=-0.52, n=30-38; Fig. 6D-F). These data suggested that PAE enhanced interneuron migration in a cell-autonomous manner. As CXCR4 is important for neuronal migration [65] and we found its expression increased in ARX^{PAE} GEOs at 120 DIV, we next explored if CXCR4 inhibition is sufficient to reduce the enhanced migration observed in ARX^{PAE} assembloids. To test that hypothesis, after 15-hour baseline recording, control and ARX^{PAE} assembloids were exposed to AMD3100, a CXCR4 inhibitor, and interneuron migration was evaluated for another 15 hours (Fig. 6A, Experimental Design 2). AMD3100 reduced interneuron migration in ARX^{PAE} assembloids to control levels (P= 0.0010, n=63-66; Fig. 6E).

Overall, our results indicated that PAE affects interneuron differentiation and migration, and produce an increase in CXCR4/CXRL12 expression.

Impact of PAE on neuronal activity

We next explored whether the cellular and molecular changes observed in COs and GEOs derived from patients with PAE in *ARX* affect neuronal activity. We performed patch-clamp recording in control and ARX^{PAE} assembloids 29–53 days after fusion. 30% of the neurons recorded did not generate action potentials, instead they exhibited small depolarizing events. 70% of the neurons exhibited firing properties and were broadly classified as either bursting or regular-spiking while held at -60 mV. Interestingly, a subset of regular-spiking cells exhibited a late-firing phenotype when held at -80 mV, (Fig. S13A). No differences in the proportion of these electrophysiologically-defined cell types were found between control and ARX^{PAE} assembloids. Moreover, we did not find differences in the intrinsic properties of the neurons between control and ARX^{PAE} assembloids (Fig. S13B-D). We next used multielectrode array (MEA) recordings to examine extracellular neural activity (Fig. 7). To compare network-wide activity between control and ARX^{PAE} organoids throughout *in vitro* neurodevelopment, MEA recordings were conducted at two time points: 120 DIV (early development) and 365 DIV (late development) (Fig. 7A). Pronounced differences in spike and synchronous burst quantities were observed between control and

ARX^{PAE} assembloids throughout development, with hyperactivity and synchrony evident in ARX^{PAE} assembloids from the early stages (Fig. 7 B-C). We examined the impact of the GABA system in the networks at the receptor level by administering GABA and picrotoxin to each assembloid. A subtle decrease in spiking and bursting activity after GABA application, even in control organoids at an early developmental stage, indicated the heterogeneity in inhibitory/excitatory operation of the $GABA_A$ receptor within the immature neuronal network. Conversely, GABA strongly inhibited spike/burst generation in control organoids at later stages (365 DIV), suggesting that standard neuronal maturation and $GABA_A$ polarity switch transpired in control organoids. Surprisingly, GABA had no effect on spiking and bursting activity in ARX^{PAE} assembloids at 365 DIV, indicating severe irresponsiveness to GABA in the patient-derived neural network. Coupling strength was measured in one-year-old organoids after GABA and picrotoxin application (Fig. 7D). GABA did not decrease coupling strength in neurons of ARX^{PAE} organoids, while it decreased neuronal pairing in control organoids. Our data suggest that human-derived neural organoids recapitulate healthy/aberrant developmental steps in responsiveness to GABA and network development in both healthy and ARX organoids.

These data suggest that PAE might impact neuronal activity.

Altogether, our results demonstrated PAE in the second tract of ARX have context-dependent consequences in cortical cells and interneurons. While it produces a premature differentiation of RGCs and intermediate progenitor cells and loss of cortical neurons in the cortex, it affects interneuron differentiation and migration from the subpallium. These defects affect neuronal activity and may underlie the seizure activity observed in patients with PAE mutation in ARX.

Discussion

ARX is a transcription factor critical for brain development [12,14,15]. Although mutations in *ARX* have been described in patients with a broad spectrum of neurological disorders, the specific consequences of each mutation are not completely understood. Moreover, many patients suffer seizures refractory to treatment. To gain a more complete understanding of the pathobiology underlying these seizures, here we studied how PAE in the second tract of *ARX*, one of the more prevalent mutations, impacts brain development using hiPSCs derived from patients with this mutation. hiPSCs were differentiated into CO and GEO, *in vitro* models of human cortical and GABAergic development respectively, and we found that ARX affects both brain areas through distinct mechanisms. PAE promotes an increase in RGCs and intermediate progenitor cells in the cortex (dorsal progenitor cells, CO), but it stimulates interneuron

migration from subpallium regions (GEO). We identified consistent cellular and molecular changes from multiple hiPSC lines derived from three healthy controls and three patients, illustrating reproducibility across experiments, batches, and cell lines in organoid models. Our study provides crucial insights into mechanisms underlying PAE mutations and offers a potential human cellular model to develop new therapeutic interventions.

ARX is expressed in both the developing and adult brain [12,13]. During development *Arx* is expressed in dorsal progenitor cells, whereas in adults its expression is restricted to interneurons that originated in the GE [12,14,15]. In this study, we found ARX to be expressed in both proliferating progenitor cells, but also differentiated cortical neurons in COs. Consistent with murine studies, ARX was expressed in ventral progenitor cells and interneurons in GEOs, and its expression was higher in GEOs when compared to dorsal tissue. Moreover, our analysis of publicly available brain transcriptome data revealed the expression of *ARX* in both human embryonic and postnatal cortical and subpallial tissues, demonstrating its widespread expression during brain development in both dorsal and ventral compartments.

Our data also demonstrate that PAE affects *ARX* expression in a context-dependent manner, for both cell type and developmental timing. For instance, we found an increase in the number of ARX^+ cells in COs, while expression in GEOs was decreased at an early timepoint. However, we found no difference in ARX expression in more mature COs or GEOs. This contrasts with mouse studies, where a reduction in the amount of ARX protein was observed in embryos with PAE in the first or second tract of ARX [17,68]. Similarly, in adult mice with PAE in the first tract, the number of ARX^+ cells was reduced in the cortex, hippocampus, and striatum [26]. These differences suggest that PAE might affect *ARX* expression differently in mice and human. Furthermore, our data using human iPSCs with a PAE in the second tract indicate there is a transient increase in cortical ARX^+ cells during early development but a decrease in ARX expression in the subpallium for a longer time. The mechanisms affecting these changes are still unknown. Additionally, studies overexpressing ARX containing PAE have shown the presence of nuclear aggregates *in vitro* [53,54], but not *in vivo* [17,26,68] suggesting that ARX may not form nuclear inclusions under physiological conditions. Moreover, cytoplasmic expression of Arx has also been observed in mice with PAE [26,55]. Interestingly, we did not detect any nuclear inclusion or cytoplasmic expression of ARX in either COs or GEOs, indicating that a different mechanism might be involved in humans. Further analysis of ARX expression in different brain regions over time is needed to clarify how PAE affects ARX expression.

The ultimate goal is to use these mechanistic understandings to treat neurologic disorders. Antisense oligos have been proposed to efficiently restore protein levels in other genetic epilepsies, for example in

Dravet syndrome, which is due to a loss of function of *Scn1a* [69]. Our data make this approach likely untenable given that ARX^{PAE} organoids have an increase of ARX in the cortex but a reduction in the subpallium. Gene-editing, using CRISPR-Cas9 technology, is another promising approach to treat genetic diseases [70], however its efficiency in GC rich regions, like polyalanine tracts, it is likely too low for reasonable therapy. Therefore, identifying how PAE affects *ARX* expression and the cell types affected will help develop novel strategies to treat these and related neurological neurodevelopmental disorders.

RGCs are the neural stem cells in the cortex that arise from the neuroepithelium and eventually differentiate into neurons [71,72]. In our study we found that PAE in *ARX* leads to an increase in RGCs and intermediate progenitor cells along with an increase in *ARX* expression in COs at 30 DIV. We also observed a mixed expression of canonical neural progenitor markers in RGCs at 30 DIV COs with PAE. For instance, although the expression of genes such as *MKI67* (a marker of proliferation), *NESTIN* and *HES5* (neural progenitor markers) was upregulated, there was a downregulation of other canonical genes such as *PAX6* and *HES1*. Moreover, these RGCs also had a high expression of *TUBB3,* a neuronal gene, suggesting a premature differentiation of RGCs due to PAE. Our findings partially overlap with previous studies in mice where it has been shown that *Arx* KO mice have a thinner cortices and reduced numbers of $BrdU^+$ cells [13]. Moreover, abrogation of *Arx* from pallial progenitor cells decreases the number of $BrdU^+$, $Pax6^+$ and $Tbr2^+$ cells, but increases $Tuj1^+$ cells [14]. Similarly, downregulation of Arx in cortical progenitor cells produces a premature cell cycle exit, while overexpression of Arx extended the cell-cycle length of progenitor cells in mouse embryos [15].

Although we observed an increase in RGCs due to PAE, there was a significant decrease in expression of PAX6, a marker of neural stem cells. It is possible that ARX controls the expression of PAX6 through different mechanisms, where both a decrease and an increase in ARX expression inhibits *PAX6*. It has been shown that *Olig2* overexpression after *Arx* loss represses expression of *Pax6* and *Tbr2* [21]. On the other hand, Pax6 can also bind to *Arx* and *NeuroD1* [73,74] and *Pax6* KO shows an increase in *Arx*-expressing cells in the cortex [74]. We speculate that the increased expression of ARX found in ARX^{PAE} COs could be an indirect consequence of *PAX6* downregulation. Furthermore, it has also been shown that Arx interacts with several components of WNT/β-catenin pathway [75]. In fact, we found an upregulation of *SFRP1* in RGCs in ARX^{PAE} COs, which inhibits WNT signaling by interacting with WNT proteins [63,64]. Abnormal cortical morphogenesis has also been reported in *Sfrp1* KO mice [76], whereas, in humans, SFRP1 maintains quiescent progenitor cells of the subventricular zone [77]. Moreover, overexpression of *Sfrp1* produces a reduction in $Pax6^+$ cells [62]. Our data further support the interaction of ARX with the WNT signaling pathway

and we hypothesize that PAX6 reduction is mediated by *SFRP1*. We also found *DLK1* to be differentially expressed in RGCs in ARX^{PAE} COs. Interestingly, *DLK1* expression was observed in clusters with low expression of *PAX6* and *HES1*. DLK1 is a non-canonical ligand of NOTCH and inhibits NOTCH signaling [60,61]. DLK1 has also been found in a population of RGCs with low expression of *SOX2* in human cortical samples [60], and it promotes the transition from proliferating progenitor cells into neurons [61]. Moreover, Dlk1 is necessary to maintain neural stem cells in the subventricular zone in mice [78]. Consistent with our results, Surmacz and colleagues have shown that overexpression of *DLK1* in human neural progenitor cells induces the expression of *TUBB3* and inhibits *HES1* expression [61]. In humans, DLK1 also promotes expression of *CDKN1C*, a cell-cycle inhibitor [61], but *Arx* KO mice exhibited an overexpression of *Cdkn1c* [14]. On the other hand, we found a reduction of *CDKN1C* levels in ARX^{PAE} COs at 30 DIV and an increase in *ARX* expression. These data suggest that in humans, both DLK1 and *CDKN1C* might be direct targets of ARX and might play a species-specific role, but additional studies are needed to confirm this hypothesis. Recent studies have shown the presence of a heterogeneous population of neuroepithelial and RGCs in human cortical tissues [60]. Our scRNA-seq data also supports heterogeneity in RGCs and suggests that ARX acts as a key transcription factor that regulates the expression of various other genes to guide neuronal differentiation. RGCs are greatly expanded in human brain and some of these subpopulations of RGCs are not present in mice, highlighting the importance of carefully selecting and interpreting models as ARX appears to play different roles in mice and humans. This may also explain why mouse models only partially recapitulate the role of ARX during human development.

We also found that the premature differentiation of RGCs in ARX^{PAE} COs leads to depletion of progenitor cells and to reduction of cortical neurons at later timepoints. Although neuronal cortical defects have not been studied in PAE mouse models or patients, defects in the organization of pyramidal neurons have been reported in patients with X-linked lissencephaly with abnormal genitalia (XLAG) [79] and in *Arx* KO mice [13]. Moreover, reduction of upper-layer cortical neurons has been shown in *Arx* cKO mice postnatally [14]. These data suggest that both KO mutations and PAE in ARX produce a reduction in cortical neurons. Furthermore, these cortical defects might play a role in the behavioral alterations observed in patients and in *Arx* cKO mice [22].

A reduction of GABAergic interneurons has been observed in the cortex of both KO mice and PAE models [17-20,23,26], as well as in zebrafish larvae [80]. Patient with XLAG also have reduced numbers of interneurons [79]. As interneurons originate in the GE and migrate tangentially, the reduction of interneurons in the cortex suggests that ARX affects neuronal migration [49,66]. In fact, accumulation of cells in the GE was observed

after inactivation or overexpression of *Arx* [13,15,23]. Moreover, aberrant migration of *Arx* KO cells was found in forebrain slice culture [16]. Lee and colleagues used a neurosphere migration assay to analyze the migration of mouse neural progenitor cells isolated from telencephalic vesicles and found that PAE in the first tract, but not in the second tract, inhibits neuronal migration [23]. Our results show that human PAE in the second tract at first compromises GABAergic differentiation and then promotes neuronal migration to the cortex. Our time-lapse experiments demonstrate that DLX1/2-GFP$^+$ interneurons with PAE migrated further and faster into cortical tissues in a cell-autonomous manner (as shown by inter-individual assembloid experiments). However, that accelerated migration did not result in an increased number of interneurons in the cortex. It is possible that interneurons with PAE keep moving because they failed to encounter their final target, or because they lacked crucial stop signals. Interestingly, migrating interneurons, after reaching the cortex, upregulate the K^+/Cl^- exchanger KCC2, which acts as a stop signal to reduce interneuron mobility [81]. Although we did not see any difference in the expression of KCC2 in GEOs by scRNA-seq (data not shown), we cannot exclude that PAE in *ARX* inhibits KCC2 expression in DLX1/2-GFP$^+$ interneurons. However, we did observe an increased expression of CXCR4 in GEOs and CXCL12 in COs. CXCR4/CXCL12 signaling is critical for interneuron migration [51,52,65,82]. Moreover, when a CXCR4 blocker was added to human assembloids, similar to the assembloids presented in this study, the migration velocity of interneurons was decreased [30]. CXCR4 is a direct target of ARX, which promotes its expression [20,83]. Thus, it is possible that PAE enhances the binding capacity of ARX to CXCR4, promoting its expression and accelerating neuronal migration. In fact, ADM3100, a CXCR4 inhibitor, was sufficient to reduce migration in ARX^{PAE} assembloids to control levels, while it did not affect interneuron migration in controls. These findings suggest that, although there are other mechanisms affecting interneuron migration, PAE in ARX promotes migration mostly through CXCR4 signaling.

Patients with PAE in *ARX* frequently develop epilepsy, among other neurological manifestations [84,85]. It has been proposed that a defect in interneuron numbers or functions was the main cause for seizure development in mouse models of PAE [18,19], while cortical defects contribute to other behavioral phenotypes [22]. Human organoid models display complex neuronal oscillations that resemble human brain activity providing an opportunity to model human cortical function in various disease states [36,86]. Our results demonstrate that both control and ARX^{PAE} assembloids contained mature neurons in comparable proportion with similar intrinsic properties. Our MEA results reveal heightened activity in ARX^{PAE} organoids, characterized by increased spikes and bursts recorded from the extracellular space. This elevated activity occurs (abnormally) synchronously in ARX^{PAE} organoids, resembling a pattern indicative of seizures—a condition typically marked by an imbalanced pattern of action potential generation within

a neural network[87,88]. According to our findings, the spontaneous hyper spike/burst generation in ARX^{PAE} organoids initiates at 120 DIV and continues through 365 DIV. The synchronous activity in the developing brain starts early in network formation, potentially leading to GABA-mediated giant action potential generation in the growing hippocampus[89] and cortex, both *in vivo*[90] and *in vitro*[91]. However, this simultaneous activity evolves into separated, in addition to organized synchronous communication between neurons for coding, pattern generation, learning, memory, and cognition in the adult brain[92]. This network evolution naturally occurs in a healthy brain[93], while patients with congenital Alzheimer's, epilepsy[94,95], or ID may develop an imbalanced and impaired network from the outset of development[96]—something we observed in ARX^{PAE} organoids. The synchronous activity persists until later stages of development (365 DIV) with surprising irresponsiveness to exogenous GABA application in ARX^{PAE} organoids. Conversely, network activity in control organoids starts with subtle responsiveness to GABA and progresses to strong sensitivity to exogenous GABA. We observed robust responsiveness to picrotoxin, a specific $GABA_A$ blocker, in all organoids, within both developmental stages, reflecting the reliable functionality of $GABA_A$ receptors in the organoids. According to our data, not every cell in the early stage of development exhibits this responsiveness, highlighting the heterogeneous polarity switch in $GABA_A$ receptors, even in control organoids. However, over time *in vitro*, it appears that the $GABA_A$ polarity is being switched from excitatory to inhibitory correctly (similar to *in vivo* neurodevelopment[97]) within control organoids because the network activity in control organoids was strongly inhibited by GABA application in 365 DIV control organoids. On the other hand, the network activity in ARX^{PAE} organoids was not blocked through GABA exposure in 365 DIV ARX^{PAE} organoids. In conclusion, this outcome suggests that PAE in ARX can impact the GABA system, but the full extent of its influence—whether it affects $GABA_A$, $GABA_B$, KCC2, or even glutamatergic receptors—remains to be explored in future studies. It is established that the GABA system and its related receptors play a crucial role in seizure development and management. Previous research has shown that overexpression of KCC2 can rescue the epilepsy phenotype through chloride concentration adjustment[98]. Studies also indicate that artificially induced abnormal reorganization of the GABA circuit can lead to epilepsy[99] underscoring the significant role of GABA as a pioneer of synapse formation in the developmental[100].

The lack of effective treatments for ID and other neurological disorders emphasizes the need for novel therapeutics. As discussed above, antisense-oligo or gene-editing therapies may not be optimal for PAE mutations. In an attempt to find a treatment for these devastating diseases, Olivetti and colleagues identified estradiol as a potential therapeutic candidate in mice with PAE in the first tract of *Arx.* They found that in early postnatal mice (a specific time window), estradiol can prevent spasms in infancy and

seizures in adult by restoring the number of interneurons in the cortex and striatum [101]. A more recent study also confirmed that estradiol treatment reduces the number of seizures although it fails to affect other abnormal behavioral and cognitive outcomes [24]. Consistent with this, the cortical defects observed in mice have been associated with abnormal behavior in mice [22]. It is tempting to speculate that estradiol might rescue normal interneuron migration and neuronal activity in ARX^{PAE} assembloids, although it might be insufficient to correct the cortical phenotype in COs.

In summary, our results demonstrate that ARX is a critical player during brain development, and also highlight the usefulness of neural organoids in studying epilepsy and other human diseases. We present evidence that PAE in the second tract of *ARX* produces an increase of RGCs and intermediate progenitor cells which differentiate prematurely leading to an overall decrease in cortical neurons. Furthermore, PAE promotes interneuron migration which is associated with altered CXCR4 expression. Both defects in cortical and GABAergic neurons contribute to abnormal neuronal activity from the very beginning of neurodevelopment. This study provides new information for understanding the pathological mechanisms under PAE mutation and demonstrates a unique human cellular model to develop potential treatments.

Acknowledgment

This work was supported by NIH grants (U01DA054170, R01NS093992, R01NS113516, and R21AG066496) and the Robert J. Kleberg, Jr. and Helen C. Kleberg Foundation and the Semmes Foundation (to J.H.); and American Epilepsy Society and LGS foundation Postdoctoral Fellowship (to V.N.-E.). We would like to thank Raul Wilshire, Mia Soerensen and Yanessa Vitela for their technical support, and Sean C. Goetsch and Jay W. Schneider for their initial help with PSC cultures. We also thank Eric D. Marsh (CHOP), Cheryl Shoubridge (The University of Adelaide) and Mary-Colette Lybrand for patient recruitment. We would like to thank Aline McKenzie for manuscript editing; and Eric D. Marsh (CHOP) and Jeffrey A. Golden (Cedars-Sinai) for critical discussion of the manuscript. We thank the UTSA Genomics Core and Sean Vargas for single cell library preparations. We also acknowledge the members of Research Computing Support Group at UTSA. Computational work in this manuscript was supported by High-Performance Clusters at UTSA and Texas Advanced Computing Center (TACC) at UT Austin. We also thank Drs. Morohashi and Kitamura for the ARX antibody. Some figures were created with BioRender.com.

Author contributions

Conceptualization, V.N.-E., P.V., Z.R.L., D.M.T. and J.H.; Methodology, V.N.-E., P.V., Z.R.L. and J.H.; Software, P.V.; Formal Analysis, V.N.-E., P.V., S.M., A.H., Z.R.L. and S.G.; Investigation, V.N.-E., P.V., S.M., Z.R.L., J.C., S.G.-A., C.N., S.G. and M.J.S.; Resources, C.N. and D.M.T., Writing – Original Draft V.N.-E.; Writing – Review & Editing, V.N.-E., P.V., S.M., Z.R.L. and J.H; Visualization, V.N.-E., P.V., Z.R.L. and J.H; Supervision, V.N.-E, M.G. and J.H.; Funding Acquisition, V.N.-E. and J.H.

Declaration of interests

The authors declare no competing interests

Figure legends

Figure 1. ARX expression in cortical and ganglionic eminence organoids

(A) Graph shows the percentage of ARX-expressing cells (number of ARX$^+$ cells/total number of cells) and the percentage of cells expressing ARX (number of ARX$^+$ cells expressing X marker/total number of ARX$^+$ cells) in COs at 30 and 120 DIV using scRNA-seq. **(B)** Graph shows the percentage of ARX expressing cells (number of ARX$^+$ cells/total number of cells) and the percentage of cells expressing ARX (number of ARX$^+$ cells expressing X marker/total number of ARX$^+$ cells) in GEOs at 30 and 120 DIV using scRNA-seq. **(C)** Data from fetal and postnatal brain tissue demonstrating ARX expression in different brain regions from 8 weeks post conception (PCW) to adulthood. Green dots indicate ganglionic eminences (GE) and striatum; blue dots indicate cortical tissue. Mo = months. The images show COs **(D)** and GEOs **(F)** derived from control and ARX^{PAE} hiPSCs immunostained against ARX and stained with DAPI**.** Graphs show the percentage of ARX$^+$ area in COs **(E)** and GEOs **(G)**. Scale bar = 50 µm. DIV = days *in vitro*, COs = cortical organoids, GEOs = ganglionic eminence organoids, IPCs = intermediate progenitor cells, NPCs = neural progenitor cells, oRGCs = outer radial glial cells, PCs = progenitor cells, RGCs = radial glial cells. * = $p < 0.05$, ** = $p < 0.01$, *** = $p < 0.001$. N= 13-16 organoids from 2 clones x 3 lines.

Figure 2. Poly-Alanine expansion affects radial glial cells in cortical organoids

(A) The images show control and ARX^{PAE} COs at 30 DIV immunostained against KI67 and PAX6, and stained with DAPI. **(B)** Graphs show the percentage of KI67$^+$ and PAX6$^+$ area in control and ARX^{PAE} COs at 30 DIV. **(C)** The images show *HES1* and *HES5* expression in control and ARX^{PAE} COs at 30 DIV by RNAscope. DAPI was used to label the nucleus. **(D)** Graphs show the HES1$^+$ and HES5$^+$ area divided by DAPI area in control

and ARX^{PAE} CO at 30 DIV. **(E)** The graph shows the relative *TBR2* mRNA level in control and ARX^{PAE} CO at 30 DIV measured by RT-qPCR. **(F)** UMAP plots from control and ARX^{PAE} COs at 30 DIV. Bar graph shows the percentage of cells in each cluster. **(G)** The graphs show the relative *ARX, CDKN1A, CDKN1B and CDKN1C* mRNA levels in control and ARX^{PAE} CO at 30 DIV measured by RT-qPCR. DIV = days *in vitro*, COs = cortical organoids. * = $p < 0.05$, ** = $p < 0.01$, ns = not significant. N= 9-17 organoids from 2 clones x 3 lines.

Figure 3. Poly-Alanine expansion promotes radial glial cell differentiation in cortical spheroids

(A) UMAP plots of subclustering of RGCs from control and ARX^{PAE} CO at 30 DIV. **(B)** Feature plots showing *ARX*, *NESTIN*, *HES5*, *HES1*, *PAX6*, *DLK1* and *TUBB3* expression in RGCs. Violin plots show the expression levels of *ARX*, *NESTIN*, *HES5*, *HES1*, *PAX6*, *DLK1* and *TUBB3*. **(C)** Volcano plot from differential gene expression (DGE) in RGCs. DIV = days *in vitro*, RGCs = radial glial cells. N= 3-4 organoids from 1 clone x 3 lines.

Figure 4. Poly-Alanine expansion compromise cortical neuronal differentiation and outer radial glial cell differentiation in cortical organoids

(A) The images show control and ARX^{PAE} COs at 120 DIV immunostained against PAX6, NEUROD1, CTIP2 and SATB2; and stained with DAPI. **(B)** Graphs show the percentage of $PAX6^+$, $NEUROD1^+$, $CTIP2^+$ and $SATB2^+$ area in control and ARX^{PAE} COs at 120 DIV. **(C)** The images show control and ARX^{PAE} COs at 120 DIV immunostained against VIMENTIN and FAM107A and stained with DAPI. **(D)** Graphs show the percentage of $VIMENTIN^+$ and $FAM107A^+$ area in control and ARX^{PAE} CO at 120 DIV. **(E)** UMAP plots from control and ARX^{PAE} COs at 120 DIV. Bar graph shows the percentage of cells in each cluster. Scale bar = 50 µm. DIV = days *in vitro*, COs = cortical organoids. * = $p < 0.05$, ** = $p < 0.01$, ns = not significant. N= 12-17 organoids from 2 clones x 3 lines.

Figure 5. Poly-Alanine expansion affects GABAergic differentiation in ganglionic eminence organoids

(A) The images show control and ARX^{PAE} GEOs at 30 DIV immunostained against KI67 and NKX2.1 and stained with DAPI. **(B)** Graph shows the percentage of $KI67^+$ and $NKX2.1^+$ area in control and ARX^{PAE} GEOs at 30 DIV. **(C)** UMAP plots from control and ARX^{PAE} GEOs at 30 DIV. Bar graph shows the percentage of cells in each cluster. **(D)** The images show control and ARX^{PAE} GEOs at 120 DIV immunostained against TUJ1, GABA and CXCR4; and stained with DAPI. **(E)** Graphs show the percentage of $TUJ1^+$, $GABA^+$ and $CXCR4^+$ area in control and ARX^{PAE} GEO at 120 DIV. **(F)** UMAP plots from control and ARX^{PAE} GEOs at 120 DIV. Bar graph shows the percentage of cells in each cluster. Scale bar = 50 µm. DIV = days *in vitro*, GEOs

= ganglionic eminence organoids. * = $p < 0.05$, ** = $p < 0.01$, ns = not significant. N= 8-14 organoids from 2 clones x 3 lines.

Figure 6. Poly-Alanine expansion in ARX accelerates interneurons migration in assembloids

(A) Experimental design for time-lapse experiments. Experimental design 1: GEOs were labeled using a lenti-DLX1/2b:GFP virus at 50 DIV. COs were labeled using an AAV-SYNAPSIN-mCherry. After 10 days, one CO and one GEO were fused and neuronal migration were observed over 15 hours at 90 DIV. Four conditions were studied: (1) Control CO + Control GEO, (2) ARX^{PAE} CO + ARX^{PAE} GEO, (3) Control CO + ARX^{PAE} GEO, (4) ARX^{PAE} CO + Control GEO. Experimental design 2: COs and GEOs were labeled and fused as described in experimental design 1. At 90 DIV, after 15-hour baseline recording, control and ARX^{PAE} assembloids were exposed to AMD3100, a CXCR4 inhibitor, and interneuron migration was evaluated for another 15 hours. **(B)** Representative images of DLX1/2-GFP^+ interneurons over time in control and ARX^{PAE} assembloids. **((C)** The graph shows the mean of the total distance of DLX1/2-GFP^+ interneurons in all four conditions. **(D)** The graph shows the velocity of DLX1/2-GFP^+ interneurons in all four conditions. N= 30-48 neurons from 11-17 organoids from 2 clones x 3 lines. **(E)** The graph shows the final distance of DLX1/2-GFP^+ area in COs and GEOs in control and ARX^{PAE} assembloids before and after ADM3100 exposure. N= 63-66 neurons from 23-24 organoids from 2 clones x 3 lines. * shows statistical analysis compared to controls. # shows statistical analysis compared to ARX^{PAE} assembloids. $*^{,\#}$ = $p < 0.05$, $**^{,\#\#}$ = $p < 0.01$. DIV = days *in vitro*, COs = cortical organoids, GEOs = ganglionic eminence organoids.

Figure 7. Network malfunction in ARX organoids

(A) Experimental design for MEA experiments. COs and GEOs were fused at 60 DIV and MEA analyses were performed at 120 and 365 DIV. The images show representative assembloids on MEA wells. **(C)** Sequential recording from healthy and ARX^{PAE} organoids under different conditions revealed that synchronous, elevated spiking activity in ARX^{PAE} organoids initiates at 120 DIV and persists through 365 DIV. In both developmental stages, all organoids respond to picrotoxin, a $GABA_A$ locker, indicating functional insertion of $GABA_A$ into the neuronal membrane. However, ARX organoids exhibit irresponsiveness to GABA at any developmental stage, while GABA inhibits neuronal activity, particularly in one-year old control organoids. Heterogeneity in $GABA_A$ polarity switch at early time point results in a subtle response to GABA, even in control organoids. (the vertical axis represents electrode numbers, and the horizontal axis shows 5 minutes of a 30-minutes recording). **(D)** Synchronous burst generation in networks with at least 25 paired electrodes (out of 60) at the same time (vertical axis) and spike numbers (horizontal axis) illustrate the electrophysiological dissociation of control and ARX^{PAE} organoids.

Approximately 80% of the recording from control organoids are distributed in the left-down corner, with less than 100 synchronized bursts and around 500,000 spike count (pink dashed-line, cluster 1). The remaining 20% of control recordings show a second distribution with larger synchronicity and spiking activity, observed only after picrotoxin application (pink-dashed line, cluster 2). Around 60% of recordings from ARX^{PAE} organoids exhibit the fourth distribution, characterized by the highest level of synchronous spiking and bursting activity (blue dashed-line, cluster 4), while 40% show the third distribution with higher spiking activity. n= 4 control (120DIV), 4 ARX^{PAE} (120 DIV); 2 control (365DIV); 2 ARX^{PAE} (365DIV) assembloids.

Figure S1. Human organoids generation and characterization

(A) Experimental design and culture conditions to obtain COs and GEOs from hiPSCs. Organoids were analyzed by immunostaining and scRNA-sequencing at 30 and 120 DIV. **(B)** The images show control COs at 30 DIV immunostained against PAX6 and CTIP2; and stained with DAPI. **(C)** UMAP plots from control COs at 30 DIV. **(D)** The images show control COs at 120 DIV immunostained against CTIP2, SATB2, VIMENTIN, FAM107A and HOPX; and stained with DAPI. **(E)** UMAP plots from control COs at 120 DIV. **(F)** The images show control GEOs at 30 DIV immunostained against KI67, NKX2.1 and TUJ1; and stain with DAPI. **(G)** UMAP plots from control GEOs at 30 DIV. **(H)** The images show control GEOs at 120 DIV immunostained against TUJ1, GABA and CXCR4; and stain with DAPI. **(I)** UMAP plots from control GEOs at 120 DIV. Scale bar = 50 µm. DIV = days *in vitro*, COs = cortical organoids, GEOs = ganglionic eminence organoids, NIM = Neural induction media, NM = Neural media, VIM = VIMENTIN. N= 18 organoids from 2 clones x 3 lines.

Figure S2. Gene expression in human organoids

Heatmaps show gene expression for each cluster in COs and GEOs at 30 and 120 DIV and subclustering of RGCs in COs at 30 DIV. N= 3-4 organoids from 1 clone x 3 lines.

Figure S3. hiPSCs characterization.

(A) The images show hiPSCs colonies derived from control and ARX^{PAE} patients immunostained against NANOG, SOX2, OCT4 and LIN28; and stained with DAPI. **(B)** The graph shows the percentage of hiPSCs derived from control and ARX^{PAE} patients positive for TRA1-6 and SSEA-4 analyzed by flow cytometry. **(C)** The images show agarose gels of PCR product of reprogramming vectors. **(D)** The images show a representative karyotype from control and ARX^{PAE} hiPSCs. Scale bar = 25 µm. N= 2 independent cultures from 2 clones x 3 lines.

Figure S4. Gene expression in 30 DIV COs by scRNA-seq

Combined UMAP from control and ARX^{PAE} 30 DIV COs showing the proportion of cells in each cluster and feature plots showing *ARX*, *PAX6*, *HES1*, *HES5* and *SFRP1* expression. Violin plots show the expression levels of *ARX*, *PAX6*, *HES1*, *HES5* and *SFRP1.* N= 3-4 organoids from 1 clone x 3 lines.

Figure S5. Gene expression in 30 DIV COs by scRNA-seq per line

Individual UMAP from control and ARX^{PAE} 30 DIV COs showing the proportion of cells in each cluster and feature plots showing *ARX*, *PAX6*, *HES1*, *HES5* and *SFRP1* expression per line. Violin plots show the expression levels of *ARX*, *PAX6*, *HES1*, *HES5* and *SFRP1* per line. N= 3-4 organoids from 1 clone x 3 lines.

Figure S6. Poly-Alanine expansion in ARX promotes organoid growth

(A) The representative bright field images of control and ARX^{PAE} COs at 30, 21 and 60 DIV. **(B)** Graph shows the area in control and ARX^{PAE} COs at 30 DIV, 21 and 60 DIV. **(C)** The representative bright field images of control and ARX^{PAE} GEOs at 30, 21 and 60 DIV. **(D)** Graph shows the area in control and ARX^{PAE} GEOs at 30 DIV, 21 and 60 DIV. Scale bar = 500 µm. DIV = days *in vitro*, COs = cortical organoids, GEOs = ganglionic eminence organoids. * = $p < 0.05$, ** = $p < 0.01$, *** = $p < 0.001$, ns = not significant. N= 22-30 organoids from 2 clones x 3 lines.

Figure S7. Gene expression in 120 DIV COs by scRNA-seq

Combined UMAP from control and ARX^{PAE} 120 DIV COs showing the proportion of cells in each cluster and feature plots showing *NEUROD1*, *BCL11B*, *FAM107A* and *CXCL12* expression. Violin plots show the expression levels of *NEUROD1*, *BCL11B*, *FAM107A* and *CXCL12.* N= 3-4 organoids from 1 clone x 3 lines.

Figure S8. Gene expression in 120 DIV COs by scRNA-seq

Individual UMAP from control and ARX^{PAE} 120 DIV COs showing the proportion of cells in each cluster and feature plots showing *NEUROD1*, *BCL11B*, *FAM107A* and *CXCL12* expression per line. Violin plots show the expression levels of *NEUROD1*, *BCL11B*, *FAM107A* and *CXCL12* per line. N= 3-4 organoids from 1 clone x 3 lines.

Figure S9. Gene expression in GEOs by scRNA-seq

(A) Combined UMAP from control and ARX^{PAE} 30 DIV GEO showing the proportion of cells in each cluster and feature plots showing ARX expression. Violin plots show the expression levels of *ARX.* **(B)** Combined UMAP from control and ARX^{PAE} 120 DIV GEOs showing the proportion of cells in each cluster and feature plots showing *GAD1*, *GAD2* and *CXCR4* expression. Violin plots show the expression levels of *GAD1*, *GAD2* and *CXCR4.* N= 3-4 organoids from 1 clone x 3 lines.

Figure S10. Gene expression in GEOs by scRNA-seq

(A) Individual UMAP from control and ARX^{PAE} 30 DIV GEOs showing the proportion of cells in each cluster and feature plots showing ARX expression per line. Violin plots show the expression levels of *ARX.* Violin plots show the expression levels of *ARX* per line. **(B)** Individual UMAP from control and ARX^{PAE} 120 DIV GEOs showing the proportion of cells in each cluster and feature plots showing *GAD1*, *GAD2* and *CXCR4* expression per line. Violin plots show the expression levels of *GAD1*, *GAD2* and *CXCR4* per line. N= 3-4 organoids from 1 clone x 3 lines.

Figure S11. Poly-Alanine expansion does not affect the number of migrating interneurons in assembloids

(A) The images show control and ARX^{PAE} assembloids at 90 DIV, 30 days after fusion, immunostained against mCherry and GFP; and stained with DAPI. COs were infected with an AAV-hSYNAPSIN-mCherry virus at 50 DIV, 10 days before fusion. GEO were infected with a lenti-DLX1/2b:GFP virus at 50 DIV, 10 days before fusion **(B)** The graph shows the percentage of DLX1/2-GFP^{+} area in COs and GEOs in control and ARX^{PAE} assembloids. . COs = cortical organoids, GEOs = ganglionic eminence organoids. Scale bar = 50 µm. N= 30-48 neurons from 11-17 organoids from 2 clones x 3 lines.

Figures S12. Poly-Alanine expansion in ARX accelerates interneurons migration in assembloids.

(A) The graph shows single tracks of DLX1/2-GFP^{+} interneurons over time in control and ARX^{PAE} assembloids. **(B)** The graph shows the mean distance at each timepoint of DLX1/2-GFP^{+} interneurons over time in all four experimental conditions. **(C)** The graph shows the distribution of the total distance of DLX1/2-GFP^{+} interneurons in all four experimental conditions. **(D)** The graph shows the percentage of mobile and immobile DLX1/2-GFP^{+} interneurons in all four experimental conditions. COs = cortical organoids, GEOs = ganglionic eminence organoids.

Figure S13. CO-GEO assembloids contain functionally mature neurons.

(A) Left: Pie chart indicated the proportion of electrophysiological cell types encountered in CO-GEO assembloids (N=63 neurons). Right: Example of spontaneous activity recorded from a neuron at rest. **(B)** No significant differences in electroresponsive properties of neurons recorded from ARX^{PAE} (n=13 cells from 4 organoids) and control assembloids (n=12 cells from 4 organoids) with respect to resting membrane potential (left) or input resistance (right). **(C)** Active membrane properties were similar across ARX^{PAE} and control assembloid neurons as assessed by spike threshold, spike amplitude, spike width, and number of current-evoked spikes. **(D)** Top: Example trace of spontaneous postsynaptic currents recorded in voltage-clamp at -40mV. Bath application of kynurenic acid blocked sEPCSs, while further addition of

picrotoxin (GABAa antagonist) and tetrodotoxin (TTX: voltage-gated sodium channel blocker) blocked sIPSCs and action potentials, respectively. Bottom: Quantification of sEPSC and sIPSC frequency (top) and amplitude (bottom) shows no group differences (Control: n = 7 cells from 2 organoids; ARX^{PAE}: n=11 cells from 3 organoids).

Video 1: Migration of DLX1/2-GFP$^+$ interneurons in control assembloids. Example 1

The video show DLX1/2-GFP$^+$ interneurons migrating in the CO side of a control assembloid.

Video 2: Migration of DLX1/2-GFP$^+$ interneurons in control assembloids. Example 2

The video show DLX1/2-GFP$^+$ interneurons migrating in the CO side of a control assembloid.

Video 3: Migration of DLX1/2-GFP$^+$ interneurons in ARX^{PAE} assembloids. Example 1

The video show DLX1/2-GFP$^+$ interneurons migrating in the CO side of a ARX^{PAE} assembloid.

Video 4: Migration of DLX1/2-GFP$^+$interneurons in ARX^{PAE} assembloids. Example 2

The video show DLX1/2-GFP$^+$ interneurons migrating in the CO side of a ARX^{PAE} assembloid.

Tables

Table 1: hiPSC lines used

Subject	Gender	Age	Number of Poly-Ala	Clinical summary
Control 1	Male	5.5 y	PA2: 12	Healthy
Control 2	Male	7.5 y	PA2: 12	Healthy
Control 3	Male	35 y	PA2: 12	Healthy
Patient 1	Male	5.5 y	PA2: 12 + 8	Intellectual disability, medically refractory epilepsy
Patient 2	Male	17 y	PA2: 12 + 8	Intellectual disability
Patient 3	Male	42 y	PA2: 12 + 8	Intellectual disability, epilepsy

Table 2: List of primary antibodies

Antibody	Host Species	Company	Cat. Number	Dilution
Anti-AC3	Rabbit	Cell Signaling	9661	1:400
Anti-ARX	Rabbit	Gift from Drs. Morohashi and Kitamura		1:500
Anti-CTIP2	Rat	Abcam	AB18465	1:300
Anti-CXCR4	Rabbit	Invitrogen	PA3-305	1:1000
Anti-DCX	Guinea pig	Millipore	AB2253	1:1000

Anti-FAM107A	Rabbit	Sigma	HPA055888	1:500
Anti-GABA	Rabbit	Sigma	A2052	1:1000
Anti-GFP	Chicken	AvesLab	GFP-120	1:500
Anti-HOPX	Rabbit	Sigma	HPA030180	1:1000
Anti-Ki67	Mouse	BD	550609	1:500
Anti-LIN28	Rabbit	Cell Signaling	3978	1:1000
Anti-NANOG	Mouse	Thermoscientific	MA1-017	1:500
Anti-NESTIN	Mouse	Millipore	MAB353	1:250
Anti-NKX2-1	Rabbit	Abcam	ab133737	1:500
Anti-NEUROD1	Goat	Santa Cruz	sc-1084	1:500
Anti-mCherry	Mouse	Invitrogen	M11217	1:1000
Anti-Oct3/4	Mouse	Santa Cruz	sc-5279	1:1000
Anti-PAX6	Rabbit	Biolegend	901301	1:300
Anti-SATB2	Rabbit	Abcam	AB34735	1:500
Anti-SOX2	Rabbit	Millipore	AB5603	1:1000
Anti-TUJ1	Mouse	Sigma	T8660	1:400
Anti-Vimentin	Chicken	Abcam	Ab24525	1:500

1

Table 3: List of primers for RT-qPCR		
Gene	**Forward**	**Reverse**
ARX	GTTCCGACACCCAGCTTTCATCAG	TGCCACTGCGCCCTCCAC
CDKN1A	CAGGGGAGCAGGCTGAAGGGT	AGAAGATCAGCCGGCGTTTGGA
CDKN1B	CGGAGCAATGCGCAGGAATAAG	GGCATTTGGGGAACCGTCTGA
CDKN1C	CGGCGCGGCGATCAAGAAG	GACACGGCGCGGGGACATC
TBR2	AAATGGGTGACCTGTGGCAAAGC	GTCTCATCCAGTGGGAACCAGTATTAGG

2 # Methods

3 ## Pluripotent Stem Cell Generation and Maintenance

4 A total of six human induced pluripotent stem cell (hiPSC) lines (Table 1) were generated from blood
5 collected from three control subjects and three ARX^{PAE} patients using an episomal reprogramming kit
6 (Invitrogen) or CytoTune-iPS Sendai Reprogramming kit (Thermofisher) and two clones per line were used.
7 Approval for the study was obtained from the University of Texas at San Antonio IRB panel and informed

consent was obtained from all subjects. Pluripotency markers were confirmed by immunocytochemistry and flow cytometry; and normal karyotype and absent of mycoplasma was maintained throughout the study in all hiPSC lines (Figure S3). We also confirmed no integration of reprogramming genes. hiPSCs were maintained in mTeSRTM1 medium (Cat. No. 05851, Stemcell Technologies) on six-well plates (Cat. No. 3506, Corning) coated with growth factor-reduced Matrigel (Cat. No. 356230, BD Biosciences) and adding ROCK inhibitor (final concentration 10 µM, Cat. No. S-1049, Selleck Chemicals). The cells were maintained with daily medium change without ROCK inhibitor until they reached 70% confluency. Then, they were detached using versene solution (Cat. No. 15040-066, Thermo Fisher Scientific) and plated 1:10.

Genotyping

Poly-alanine expansion on the second tract of *ARX* were confirmed by sequencing. Genomic DNA was extracted from hiPSCs using DNeasy® Blood & Tissue Kit (QIAprep #69504) following manufacturer's instructions. OneTaq® Hot Start DNA Polymerase (New England BioLab Cat. No. M0481) was used to amplify the second alanine tract of *ARX* using forward (GGGGGCCGCCTCCTTCAG) and reverse (CCTGGTGAAGACGTCCGGGTAGTG) primers. PCR conditions were as follow, 94 °C for 4 minutes; 94 °C 30 sec, 60 °C 30 sec, 68 °C 1 minute for 35 cycles; 68 °C 5 minutes. PCR products (798 bp) were visualized on an agarose gel and sent for Sanger sequencing.

Organoid Culture

Human cortical organoids (CO) and human ganglionic eminence organoids (GEO) were generated using the method described by Pasca and colleagues with slight modifications [30,33]. Briefly, hiPSCs were dissociated using accutase (Sigma) and 9,000 cells were resuspended in 150 µl neural induction medium (DMEM/F12, 20% knock-out serum replacement, Glutamax, MEM-NEAA, 0.1 mM 2-mercaptoethanol, penicillin/streptomycin) containing Y27632 (20 µM). Media was changed daily. On days 1-5, the SMAD inhibitors, dorsomorphin (5 µM, Sigma) and SB-431542 (10 µM, Tocris) were added. On days 6-24, media was replaced with neural medium (Neurobasal A, B-27 without Vitamin A, Glutamax, penicillin/streptomycin) containing the growth factors, bFGF (20 ng/ml, Peprotech) and EGF (20 ng/ml, Peprotech). On day 25, organoids were transferred to neural medium containing BDNF (20 ng/ml, Peprotech) and NT-3 (20 ng/ml, Peprotech) until day 42. GEOs also received the Wnt pathway inhibitor, IWP-2 (5 µM, Selleckchem) on days 4-22 and the Smo pathway activator, SAG (100 nM, Selleckchem) on days 12-22 (Fig S1A). After day 25, organoids were maintained on an orbital shaker to promote oxygenation.

Interneuron Migration

On day 50, GEOs were infected with lentivirus hDlx1/2b:GFP (gift from Dr. John Rubenstein) and CO with an AAV-DJ1-hSYN1:mCherry (Stanford Gene Vector and Virus Core at Stanford University School of Medicine). On day 60, one GEO and one CO were transferred to a well of a 24-well plate and placed in close contact, containing neural media and incubated without disruption for 3-4 days. On day 90, assembloids were transferred to glass-bottom plates (Corning) and the migration of hDLX1/2b:GFP interneurons into cortical tissue was recorded under environmentally controlled conditions (37 °C, 5% CO2). Time-lapse images were taken every 20 min for 15 hours using a confocal Leica Microscope with a motorized stage (TCS SPE8) (Fig. 7A). In each field, we took images every 3 µm up to 150-200 µm thickness. Only neurons that did not move out of the field during the recording time were analyzed. Organoids with major drift were discarded. Some assembloids were fixed, sliced, and imaged. Image J was used to determine the distance and the average velocity of the hDLX1/2b:GFP cells when mobile. Videos were processed using Leica software.

Immunohistochemistry

Organoids were fixed in 4% paraformaldehyde overnight at 4 °C and incubated in 30% sucrose for 48 hours at 4 °C. Then, organoids were embedded in OCT compound and frozen. A cryostat was used to cut 14-µm sections, which were mounted on slides. For immunohistochemistry, slides were incubated in blocking solution (0.3% Triton X-100, 3% normal goat serum in TBS) for 1 hour at room temperature, and primary antibody (Table 2) overnight at 4 °C in a humidified chamber. After washing three times, slides were incubated in secondary antibody (Jackson Immunoresearch, 1:500) for 2 hours at room temperature. Slides were washed, 4',6-diamidino-2-phenylindole (DAPI; Sigma, Cat. No. D9542) was added to label nuclei, then coverslipped using polyvinyl Alcohol solution (PVA; Sigma, Cat. No. BP168-122). Four sections per organoids were imaged using a Leica Microscope (Spe8Info) and fluorescence intensity was analyzed using Image J software.

RNAscope

RNAscope was performed on cryostat sections following manufacturer's instructions with antigen retrieval (ACDBio). Human probes were custom-made by ACDBio for *HES1* and *HES5* mRNA. Four sections per organoids were imaged using a Leica Microscope (Spe8Info) at 40x oil immersion objective. Quantification was performed using CellProfiler. Data are shown as the ratio of *HES1* or *HES5* mRNA to DAPI expression.

Dissociation of organoids and single cell RNA sequencing (scRNA-seq)

For single-cell dissociation and RNA seq, COs and GEOs were dissociated using Worthington papain dissociation kit (Cat. No. LK003150) per the instruction manual. Each developmental timepoint (30 DIV and 120 DIV) and each subtype of organoid (cortical and ganglionic eminence) was processed separately. A total of 3 lines, and one clone per line, were used for each condition. Briefly, 3-4 organoids for each timepoint and subtype were collected in a small petri dish with 5 ml of prewarmed Worthington papain solution and 250 µl of Worthington DNase solution. The organoids were chopped into small pieces using sterile blades and the dishes were placed on a digital rocker in a cell culture incubator for 60 minutes at 37 °C. Digested tissue was collected in a 15-ml tube and 5 ml of room temperature Earle's Balanced Salt Solution (EBSS) was added. The mixture was then triturated by gently pipetting up and down 10 times with 10-ml plastic pipette followed by 1-ml and 200-µl pipettes. Any undissociated tissue was allowed to settle at the bottom of the tube and the cloudy suspension was carefully aspirated in a clean 15-ml tube. Next, 3.15 ml of inhibitor solution (2.7 ml of EBSS, 300 µl of reconstituted Worthington albumin-ovomucoid solution and 150 µl of DNase solution) was carefully layered over the cloudy suspension and tubes were centrifuged at 300 g for 5 minutes at room temperature. The supernatant was carefully discarded, and cell pellet was gently suspended in 500 µl of cold neurobasal A media. Cell viability was determined using trypan blue.

10x Genomics single cell libraries were generated by the University of Texas at San Antonio (UTSA) Genomics Core. Cell suspensions were loaded into 10x Genomics microfluidics chips from Chip B Single Cell kit (Cat. No. 1000153) and onto the 10x Chromium controller to capture single cells in Gel Beads-in-emulsion (GEMs). 7,000 cells/sample were targeted for capture in GEMs preceding library prep following manufacturer's recommendations for 10x Genomics 3' Gene Expression Reagent kit (Cat. No. 1000269) with v3 chemistry. Sequencing was performed on either NextSeq 500 at University of Texas Health Science Center (UTHSC) at San Antonio or NovaSeq 6000 at North Texas Genome Center (NTGC) to generate 50,000 reads/cell in each sample.

scRNA-seq data analysis

Cell Ranger from 10x Genomics and Seurat were used for all scRNA-seq data analysis as described below. Base calls for each sample were converted into FASTQ reads using cellranger mkfastq. FASTQ reads were aligned to the GRCh38 -3.0.0 human reference genome assembly and cell-by-gene count matrices were generated using cellranger count function with default parameters except '--expect-cells' set to 8,000. Libraries for Control 1 and ARX^{PAE} 1 at COs 120 DIV were re-sequenced to increase the read depths and

files were aggregated using cell ranger. All further analysis was performed using Seurat v.3.2 in in R (v.3.6.0) or Seurat v.4.0 in R (v.4.0.3) [102,103]. Briefly, for each timepoint (30 DIV and 120 DIV) and organoid subtype (cortical and ganglionic eminence), SeuratObject was initialized for controls (Control 1, Control 2, Control 3) and ARX^{PAE} (ARX^{PAE} 1, ARX^{PAE} 2, ARX^{PAE} 3) separately using filtered feature matrices. Genes that were expressed in ≥10 cells (min.cells=10) and cells with at least 500 detected genes (min.features = 500) were used as filtering parameters for creating each SeuratObject. Next, all six SeuratObjects were merged together using merge function from Seurat to create a single SeuratObject for all further analysis. Mitochondrial and ribosomal genes were calculated and cells with nFeature_RNA>500 and nFeature_RNA<6000 were retained after further filtering and quality control. Unique molecular identifier (UMI) counts were normalized for each cell by the total expression multiplied by 10^6 and log-transformed. Variable genes were identified using mean.var.plot method in Seurat and ScaleData function was used to regress out all the unwanted sources of variations including mitochondrial and ribosomal genes. Principal Component Analysis (PCA) was run on scaled data and the top principal components (PCs) were chosen based on Seurat's ElbowPlots (19 PCs were chosen for each merged SeuratObject). RunHarmony function from harmony package (v.0.1.0) was used for batch correction and cells were clustered in PCA space using Seurat's FindNeighbors function with reduction='harmony' and dims=1:30 followed by FindClusters with resolution=0.5. Uniform manifold approximation and projection (UMAP) in Seurat was finally used as a non-linear dimensionality reduction technique to visualize and further explore the cells in each dataset.

Upregulated genes in each cluster were identified using the VeniceAllMarker tool from Signac package (v.1.3.0) from BioTuring (https://github.com/bioturing/signac). Cell types were assigned based on top marker genes in each cluster. DoHeatmap function from Seurat was used for creating heatmaps representing the expression of genes used to identify cell types. Celltype proportion in each dataset was calculated using glmer function from R package lme4 (v.1.1.27.1) and the script was adapted from [104]. For RGCs in 30 DIV cortical organoid dataset, cells were further subclustered and differential gene expression analysis was performed using FindMarkers function from Seurat with default parameters. EnhancedVolcano (v.1.8.0) package in R was used to create the volcano plot for differentially expressed genes in RGCs.

The datasets presented in this study can be found in NIH repositories (accession number GSE215362). The codes used in this study can be found on https://github.com/parulvarma123/ARX_Organoids_scRNAseq.

RNA isolation, RT-PCR and quantitative PCR

Organoid RNA was extracted using the Qiagen RNeasy Micro Kit according to manufacturer instructions. The concentration and purity of the RNA samples were measured by using Nano-drop (Thermo Fisher Scientific). The extracted RNA (500 ng) was reverse transcribed according to the protocol supplied with SuperScriptIII First-Strand Synthesis System for RT-PCR (Catalog# 18080-051, Invitrogen Life Technologies). Quantitative real-time PCR (qRT-PCR) was carried out using ViiA (Applied Biosystems, Foster City, CA, USA). Reactions were run in triplicate and expression of each gene were normalized to the geometric mean of GAPDH as a housekeeping gene and analyzed by using the ΔΔCT method. The primer sequences of each gene are listed in Table 3.

Electrophysiology.

Assembloids (29–53 days after fusion) were prepared for electrophysiological recordings by embedding in a low-melting point 4% agarose (Fisher Scientific Cat. No. 16520050) block and briefly incubated in partially frozen aCSF containing (in mM): 126 NaCl, 2.5 KCl, 1.25 NaH2PO4, 10 Dextrose, 2 $CaCl_2$, 1 $MgSO_4$, 26 NaHCO3, 1.3 Na-ascorbate, and 0.6 Na-pyruvate, and equilibrated with 95% O_2 and 5% CO_2 (pH. 7.2, 300 mOsm). Slices were made at 250-µm thickness with a Leica VT1000s vibratome and placed in an incubation chamber containing aCSF (in mM): 126 NaCl, 2.5 KCl, 1.25 NaH2PO4, 10 dextrose, 2 $CaCl_2$, 1 $MgSO_4$, 26 $NaHCO_3$, equilibrated with 95% O_2 and 5% CO_2 at 37°C for 30 minutes, before gradually returning to room temperature. Recordings were performed at 32°C. Neurons were identified by their large cell bodies using DIC optics (Nikon Eclipse fn1). Recordings targeted CO neurons located close to the site of fusion. Recording electrodes were pulled from thick-walled borosilicate glass had a resistance of 4–6 MΩ when filled with internal solution. We followed the procedures described in [30] and used a low-chloride internal pipette solution containing: 145 mM K-gluconate, 0.1 mM $CaCl_2$, 2.5 mM $MgCl_2$, 10 mM HEPES, 0.2 mM EGTA, 4mM Na-phosphocreatine, to record both ePSCs and IPSCs while holding the cell at -40 mV. Data were collected using a 1550B digitizer (Molecular Devices), a 700B patch-clamp amplifier (Molecular Devices) and acquired with the pClamp 10.6 software (Molecular Devices). Recordings were filtered at 10kHz. Recordings of spontaneous currents were analyzed using Neuroexpress [105]. Electroresponsive properties of organoid neurons were assessed by holding cells, each cell at –60 mV and delivering gradually increasing current injections (-10 pA to 20 pA in 5 pA steps; 500 ms duration). Pharmacological characterization of postsynaptic currents was performed by bath application of kynurenic acid (1 mM), picrotoxin (100 µM), and tetrodotoxin (500 nM). Data was analyzed using Graphpad Prism.

Multi-Electrode Array (MEA) Assay

All electrophysiological recordings were carried out inside a humid (i.e., 95% R.H.) incubator at 37°C and 5% CO2. The brain organoids were maintained using BrainPhysTM hPSC Neuron kit (05795; STEMCELL Technology) through the days immediately preceding the recording sessions. For each session, individual organoids were placed on either the 3D (60-3DMEA200/12/80iR-Ti, Multichannel system, Harvard Bioscience) or 2D commercially available Microelectrode Arrays (MEAs) (60MEA200/30iR-Ti, Multichannel systems, Harvard Bioscience). To ensure optimal attachment to the MEA surface, 200 µL of BrainPhysTM hPSC Neuron media was also bath applied. Sequential recordings were then performed on each organoid, as it follows: baseline conditions, 100 µM glutamate (6106-04-3, Sigma-Aldrich), 20 µM GABA (56-12-2, Sigma-Aldrich), and finally 58 µM picrotoxin (124-87-8, Sigma-Aldrich). These chemicals were applied to the culture medium, and careful media exchange occurred every 45 minutes to prevent organoid movement on the electrodes. Recording of electrical activity from each of individual microelectrode of the MEA started 10 minutes after the chemical application, allowing their full dilution in the medium and discarding artifacts and transient responses. To prevent media evaporation and optimize recording conditions, each MEA was sealed with fluorinated Teflon thin film (MEA-MEM-set5, Multichannel systems, Harvard Bioscience) that selectively allows gas permeability but block water evaporation and microorganisms contamination. Each recording session lasted 30 minutes. Each 2DMEA featured 60 Titanium nitrate (TiN) microelectrodes, with 30 µm of diameter, arranged in a uniform 8 x 8 layout with a 200 µm inter-electrode pitch. Similarly, each 3DMEA featured 60 TiN microelectrodes with 50 µm diameter and 100 µm pitch, but were organized in 3D with a height of 80 µm. Raw electrical potentials, detected extracellularly from each microelectrode, were amplified using an electronic amplifier (ME2100-Mini, Multichannel systems, Harvard Bioscience), sampled at 25 kHz/channel, and digitized at 16 bits resolution. The recorded extracellular potential traces were stored on disk via software (Experimenter, Multichannel systems, Harvard Bioscience) for subsequent offline analyses. To detect the time of occurrence of putative action potentials (i.e. spike times), a peak detection algorithm with adaptive threshold was employed, so that spontaneous network-wide synchronization of spike times, i.e., network bursts[106,107] could be detected and quantified The events detected over time at each distinct MEA microelectrode were visualized as a raster plot and further analyzed by conventional spike train analysis[106,107]. The degree of functional interaction between pairs of MEA microelectrodes was derived using conventional cross-correlation analysis of spike times[108], limited to inter-spike delays less than 500 ms and quantified by 3 ms bins. To account for firing rate modulation, a normalization procedure divided each cross correlogram by the square root of the product of the number of spikes in either of the spike

trains. The peak value from the cross correlogram represented the connectivity strength of the electrode pairs. Distributions of these peak values across various experimental conditions were generated to facilitate a comparison of coupling strength.

Human Fetal Brain Tissue Analysis

Fetal brain bulk RNA sequencing dataset was downloaded from BrainSpan: Atlas of the Developing Human Brain (https://brainspan.org/). RPKM (reads per kilobase transcripts per million mapped reads) values for *ARX* gene were mined and normalized for each sample using the following formula RPKM(gene)/(∑RPKM(all genes in the sample)) X 10^6. Graphpad Prism was used to plot ARX normalized counts from 8 weeks post-conception (wpc) to 40 years of age.

Statistical analysis

Outliers were removed from each dataset using GraphPad Prism software (Q=1%). A two-tailed Student's *t*-test was used to compare the mean ± standard error of the mean (SEM) values, with Welch´s correction when the F-test indicated significant differences between the variances of both groups. All analyses were carried out with GraphPad Prism software and the differences were considered as statistically significant when $P<0.05$. Effect size (d) was calculated using: https://www.psychometrica.de/effect_size.html. A large effect size was considered when $d \geq 0.8$.

References

1 Marsh, E. D. & Golden, J. A. in *Jasper's Basic Mechanisms of the Epilepsies* (2012).

2 Miura, H., Yanazawa, M., Kato, K. & Kitamura, K. Expression of a novel aristaless related homeobox gene 'Arx' in the vertebrate telencephalon, diencephalon and floor plate. *Mech Dev* **65**, 99-109, doi:10.1016/s0925-4773(97)00062-2 (1997).

3 Olivetti, P. R. & Noebels, J. L. Interneuron, interrupted: molecular pathogenesis of ARX mutations and X-linked infantile spasms. *Curr Opin Neurobiol* **22**, 859-865, doi:10.1016/j.conb.2012.04.006 (2012).

4 Friocourt, G. & Parnavelas, J. G. Mutations in ARX Result in Several Defects Involving GABAergic Neurons. *Front Cell Neurosci* **4**, 4, doi:10.3389/fncel.2010.00004 (2010).

5 Scheffer, I. E. *et al.* X-linked myoclonic epilepsy with spasticity and intellectual disability: mutation in the homeobox gene ARX. *Neurology* **59**, 348-356 (2002).

6 Stromme, P., Mangelsdorf, M. E., Scheffer, I. E. & Gecz, J. Infantile spasms, dystonia, and other X-linked phenotypes caused by mutations in Aristaless related homeobox gene, ARX. *Brain Dev* **24**, 266-268 (2002).

7 Uyanik, G. *et al.* ARX mutations in X-linked lissencephaly with abnormal genitalia. *Neurology* **61**, 232-235 (2003).

8 Kato, M., Das, S., Petras, K., Sawaishi, Y. & Dobyns, W. B. Polyalanine expansion of ARX associated with cryptogenic West syndrome. *Neurology* **61**, 267-276 (2003).

9 Stromme, P. *et al.* Mutations in the human ortholog of Aristaless cause X-linked mental retardation and epilepsy. *Nat Genet* **30**, 441-445, doi:10.1038/ng862 (2002).

10 Albrecht, A. & Mundlos, S. The other trinucleotide repeat: polyalanine expansion disorders. *Curr Opin Genet Dev* **15**, 285-293, doi:10.1016/j.gde.2005.04.003 (2005).

11 Messaed, C. & Rouleau, G. A. Molecular mechanisms underlying polyalanine diseases. *Neurobiol Dis* **34**, 397-405, doi:10.1016/j.nbd.2009.02.013 (2009).

12 Colombo, E., Galli, R., Cossu, G., Gecz, J. & Broccoli, V. Mouse orthologue of ARX, a gene mutated in several X-linked forms of mental retardation and epilepsy, is a marker of adult neural stem cells and forebrain GABAergic neurons. *Dev Dyn* **231**, 631-639, doi:10.1002/dvdy.20164 (2004).

13 Kitamura, K. *et al.* Mutation of ARX causes abnormal development of forebrain and testes in mice and X-linked lissencephaly with abnormal genitalia in humans. *Nat Genet* **32**, 359-369, doi:10.1038/ng1009 (2002).

14 Colasante, G. *et al.* ARX regulates cortical intermediate progenitor cell expansion and upper layer neuron formation through repression of Cdkn1c. *Cereb Cortex* **25**, 322-335, doi:10.1093/cercor/bht222 (2015).

15 Friocourt, G. *et al.* Cell-autonomous roles of ARX in cell proliferation and neuronal migration during corticogenesis. *J Neurosci* **28**, 5794-5805, doi:10.1523/JNEUROSCI.1067-08.2008 (2008).

16 Colombo, E. *et al.* Inactivation of Arx, the murine ortholog of the X-linked lissencephaly with ambiguous genitalia gene, leads to severe disorganization of the ventral telencephalon with impaired neuronal migration and differentiation. *J Neurosci* **27**, 4786-4798, doi:10.1523/JNEUROSCI.0417-07.2007 (2007).

17 Kitamura, K. *et al.* Three human ARX mutations cause the lissencephaly-like and mental retardation with epilepsy-like pleiotropic phenotypes in mice. *Hum Mol Genet* **18**, 3708-3724, doi:10.1093/hmg/ddp318 (2009).

18 Marsh, E. *et al.* Targeted loss of Arx results in a developmental epilepsy mouse model and recapitulates the human phenotype in heterozygous females. *Brain* **132**, 1563-1576, doi:10.1093/brain/awp107 (2009).

19 Marsh, E. D. *et al.* Developmental interneuron subtype deficits after targeted loss of Arx. *BMC Neurosci* **17**, 35, doi:10.1186/s12868-016-0265-8 (2016).

20 Fulp, C. T. *et al.* Identification of Arx transcriptional targets in the developing basal forebrain. *Hum Mol Genet* **17**, 3740-3760, doi:10.1093/hmg/ddn271 (2008).

21 Lim, Y. *et al.* Arx Expression Suppresses Ventralization of the Developing Dorsal Forebrain. *Sci Rep* **9**, 226, doi:10.1038/s41598-018-36194-6 (2019).

22 Simonet, J. C., Sunnen, C. N., Wu, J., Golden, J. A. & Marsh, E. D. Conditional Loss of Arx From the Developing Dorsal Telencephalon Results in Behavioral Phenotypes Resembling Mild Human ARX Mutations. *Cereb Cortex* **25**, 2939-2950, doi:10.1093/cercor/bhu090 (2015).

23 Lee, K., Ireland, K., Bleeze, M. & Shoubridge, C. ARX polyalanine expansion mutations lead to migration impediment in the rostral cortex coupled with a developmental deficit of calbindin-

positive cortical GABAergic interneurons. *Neuroscience* **357**, 220-231, doi:10.1016/j.neuroscience.2017.06.010 (2017).

24 Loring, K. E. *et al.* Early 17beta-estradiol treatment reduces seizures but not abnormal behaviour in mice with expanded polyalanine tracts in the Aristaless related homeobox gene (ARX). *Neurobiol Dis* **153**, 105329, doi:10.1016/j.nbd.2021.105329 (2021).

25 Mattiske, T., Lee, K., Gecz, J., Friocourt, G. & Shoubridge, C. Embryonic forebrain transcriptome of mice with polyalanine expansion mutations in the ARX homeobox gene. *Hum Mol Genet* **25**, 5433-5443, doi:10.1093/hmg/ddw360 (2016).

26 Price, M. G. *et al.* A triplet repeat expansion genetic mouse model of infantile spasms syndrome, Arx(GCG)10+7, with interneuronopathy, spasms in infancy, persistent seizures, and adult cognitive and behavioral impairment. *J Neurosci* **29**, 8752-8763, doi:10.1523/JNEUROSCI.0915-09.2009 (2009).

27 Jackson, M. R. *et al.* Extensive phenotyping of two ARX polyalanine expansion mutation mouse models that span clinical spectrum of intellectual disability and epilepsy. *Neurobiol Dis* **105**, 245-256, doi:10.1016/j.nbd.2017.05.012 (2017).

28 van der Worp, H. B. *et al.* Can animal models of disease reliably inform human studies? *PLoS Med* **7**, e1000245, doi:10.1371/journal.pmed.1000245 (2010).

29 Bagley, J. A., Reumann, D., Bian, S., Levi-Strauss, J. & Knoblich, J. A. Fused cerebral organoids model interactions between brain regions. *Nat Methods*, doi:10.1038/nmeth.4304 (2017).

30 Birey, F. *et al.* Assembly of functionally integrated human forebrain spheroids. *Nature* **545**, 54-59, doi:10.1038/nature22330 (2017).

31 Di Lullo, E. & Kriegstein, A. R. The use of brain organoids to investigate neural development and disease. *Nat Rev Neurosci*, doi:10.1038/nrn.2017.107 (2017).

32 Lancaster, M. A. *et al.* Cerebral organoids model human brain development and microcephaly. *Nature* **501**, 373-379, doi:10.1038/nature12517 (2013).

33 Pasca, A. M. *et al.* Functional cortical neurons and astrocytes from human pluripotent stem cells in 3D culture. *Nat Methods* **12**, 671-678, doi:10.1038/nmeth.3415 (2015).

34 Blair, J. D., Hockemeyer, D. & Bateup, H. S. Genetically engineered human cortical spheroid models of tuberous sclerosis. *Nat Med*, doi:10.1038/s41591-018-0139-y (2018).

35 Nieto-Estevez, V. & Hsieh, J. Human Brain Organoid Models of Developmental Epilepsies. *Epilepsy Curr* **20**, 282-290, doi:10.1177/1535759720949254 (2020).

36 Samarasinghe, R. A. *et al.* Identification of neural oscillations and epileptiform changes in human brain organoids. *Nat Neurosci*, doi:10.1038/s41593-021-00906-5 (2021).

37 Pasca, S. P. *et al.* A nomenclature consensus for nervous system organoids and assembloids. *Nature* **609**, 907-910, doi:10.1038/s41586-022-05219-6 (2022).

38 Nieto-Estevez, V. *et al.* Buprenorphine Exposure Alters the Development and Migration of Interneurons in the Cortex. *Front Mol Neurosci* **15**, 889922, doi:10.3389/fnmol.2022.889922 (2022).

39 Birey, F. *et al.* Dissecting the molecular basis of human interneuron migration in forebrain assembloids from Timothy syndrome. *Cell Stem Cell*, doi:10.1016/j.stem.2021.11.011 (2021).

40 Sansom, S. N. *et al.* The level of the transcription factor Pax6 is essential for controlling the balance between neural stem cell self-renewal and neurogenesis. *PLoS Genet* **5**, e1000511 (2009).

41 Chen, B. *et al.* The Fezf2-Ctip2 genetic pathway regulates the fate choice of subcortical projection neurons in the developing cerebral cortex. *Proc Natl Acad Sci U S A* **105**, 11382-11387, doi:10.1073/pnas.0804918105 (2008).

42 Greig, L. C., Woodworth, M. B., Galazo, M. J., Padmanabhan, H. & Macklis, J. D. Molecular logic of neocortical projection neuron specification, development and diversity. *Nat Rev Neurosci* **14**, 755-769, doi:10.1038/nrn3586 (2013).

43 Leid, M. *et al.* CTIP1 and CTIP2 are differentially expressed during mouse embryogenesis. *Gene Expr Patterns* **4**, 733-739, doi:10.1016/j.modgep.2004.03.009 (2004).

44 Hansen, D. V., Lui, J. H., Parker, P. R. & Kriegstein, A. R. Neurogenic radial glia in the outer subventricular zone of human neocortex. *Nature* **464**, 554-561, doi:10.1038/nature08845 (2010).

45 Lui, J. H., Hansen, D. V. & Kriegstein, A. R. Development and evolution of the human neocortex. *Cell* **146**, 18-36, doi:10.1016/j.cell.2011.06.030 (2011).

46 Leone, D. P. *et al.* Satb2 Regulates the Differentiation of Both Callosal and Subcerebral Projection Neurons in the Developing Cerebral Cortex. *Cereb Cortex* **25**, 3406-3419, doi:10.1093/cercor/bhu156 (2015).

47 Tanaka, R. *et al.* Accurate determination of S-phase fraction in proliferative cells by dual fluorescence and peroxidase immunohistochemistry with 5-bromo-2'-deoxyuridine (BrdU) and Ki67 antibodies. *J Histochem Cytochem* **59**, 791-798, doi:0022155411411090 [pii]

10.1369/0022155411411090 (2011).

48 Butt, S. J. *et al.* The requirement of Nkx2-1 in the temporal specification of cortical interneuron subtypes. *Neuron* **59**, 722-732, doi:10.1016/j.neuron.2008.07.031 (2008).

49 Lim, L., Mi, D., Llorca, A. & Marín, O. Development and Functional Diversification of Cortical Interneurons. *Neuron* **100**, 294-313, doi:10.1016/j.neuron.2018.10.009 (2018).

50 Li, G. *et al.* Regional distribution of cortical interneurons and development of inhibitory tone are regulated by Cxcl12/Cxcr4 signaling. *J Neurosci* **28**, 1085-1098, doi:10.1523/JNEUROSCI.4602-07.2008 (2008).

51 Tiveron, M. C. *et al.* Molecular interaction between projection neuron precursors and invading interneurons via stromal-derived factor 1 (CXCL12)/CXCR4 signaling in the cortical subventricular zone/intermediate zone. *J Neurosci* **26**, 13273-13278, doi:10.1523/JNEUROSCI.4162-06.2006 (2006).

52 Wang, Y. *et al.* CXCR4 and CXCR7 have distinct functions in regulating interneuron migration. *Neuron* **69**, 61-76, doi:10.1016/j.neuron.2010.12.005 (2011).

53 Friocourt, G., Poirier, K., Rakic, S., Parnavelas, J. G. & Chelly, J. The role of ARX in cortical development. *Eur J Neurosci* **23**, 869-876, doi:10.1111/j.1460-9568.2006.04629.x (2006).

54 Nasrallah, I. M., Minarcik, J. C. & Golden, J. A. A polyalanine tract expansion in Arx forms intranuclear inclusions and results in increased cell death. *J Cell Biol* **167**, 411-416, doi:10.1083/jcb.200408091 (2004).

55 Shoubridge, C., Cloosterman, D., Parkinson-Lawerence, E., Brooks, D. & Gecz, J. Molecular pathology of expanded polyalanine tract mutations in the Aristaless-related homeobox gene. *Genomics* **90**, 59-71, doi:10.1016/j.ygeno.2007.03.005 (2007).

56 Allen, T. & Lobe, C. G. A comparison of Notch, Hes and Grg expression during murine embryonic and post-natal development. *Cell Mol Biol (Noisy-le-grand)* **45**, 687-708 (1999).

57 Chenn, A. & Walsh, C. A. Regulation of cerebral cortical size by control of cell cycle exit in neural precursors. *Science* **297**, 365-369, doi:10.1126/science.1074192 (2002).

58 Hodge, R. D. *et al.* Tbr2 expression in cajal-retzius cells and intermediate neuronal progenitors is required for morphogenesis of the dentate gyrus. *J Neurosci* **33**, 4165-4180, doi:33/9/4165 [pii]

10.1523/JNEUROSCI.4185-12.2013 (2013).

59 Hodge, R. D. *et al.* Tbr2 is essential for hippocampal lineage progression from neural stem cells to intermediate progenitors and neurons. *J Neurosci* **32**, 6275-6287, doi:32/18/6275 [pii]

10.1523/JNEUROSCI.0532-12.2012 (2012).

60 Eze, U. C., Bhaduri, A., Haeussler, M., Nowakowski, T. J. & Kriegstein, A. R. Single-cell atlas of early human brain development highlights heterogeneity of human neuroepithelial cells and early radial glia. *Nat Neurosci* **24**, 584-594, doi:10.1038/s41593-020-00794-1 (2021).

61 Surmacz, B. *et al.* DLK1 promotes neurogenesis of human and mouse pluripotent stem cell-derived neural progenitors via modulating Notch and BMP signalling. *Stem Cell Rev Rep* **8**, 459-471, doi:10.1007/s12015-011-9298-7 (2012).

62 Miao, N. *et al.* Opposite Roles of Wnt7a and Sfrp1 in Modulating Proper Development of Neural Progenitors in the Mouse Cerebral Cortex. *Front Mol Neurosci* **11**, 247, doi:10.3389/fnmol.2018.00247 (2018).

63 Bovolenta, P., Esteve, P., Ruiz, J. M., Cisneros, E. & Lopez-Rios, J. Beyond Wnt inhibition: new functions of secreted Frizzled-related proteins in development and disease. *J Cell Sci* **121**, 737-746, doi:10.1242/jcs.026096 (2008).

64 Kawano, Y. & Kypta, R. Secreted antagonists of the Wnt signalling pathway. *J Cell Sci* **116**, 2627-2634, doi:10.1242/jcs.00623 (2003).

65 Mithal, D. S., Banisadr, G. & Miller, R. J. CXCL12 signaling in the development of the nervous system. *J Neuroimmune Pharmacol* **7**, 820-834, doi:10.1007/s11481-011-9336-x (2012).

66 Letinic, K., Zoncu, R. & Rakic, P. Origin of GABAergic neurons in the human neocortex. *Nature* **417**, 645-649, doi:10.1038/nature00779 (2002).

67 Cobos, I. *et al.* Mice lacking Dlx1 show subtype-specific loss of interneurons, reduced inhibition and epilepsy. *Nat Neurosci* **8**, 1059-1068, doi:10.1038/nn1499 (2005).

68 Lee, K., Mattiske, T., Kitamura, K., Gecz, J. & Shoubridge, C. Reduced polyalanine-expanded Arx mutant protein in developing mouse subpallium alters Lmo1 transcriptional regulation. *Hum Mol Genet* **23**, 1084-1094, doi:10.1093/hmg/ddt503 (2014).

69 Han, Z. *et al.* Antisense oligonucleotides increase Scn1a expression and reduce seizures and SUDEP incidence in a mouse model of Dravet syndrome. *Sci Transl Med* **12**, doi:10.1126/scitranslmed.aaz6100 (2020).

70 Olson, E. N. Toward the correction of muscular dystrophy by gene editing. *Proc Natl Acad Sci U S A* **118**, doi:10.1073/pnas.2004840117 (2021).

71 Kwan, K. Y., Sestan, N. & Anton, E. S. Transcriptional co-regulation of neuronal migration and laminar identity in the neocortex. *Development* **139**, 1535-1546, doi:10.1242/dev.069963 (2012).

72 Noctor, S. C., Flint, A. C., Weissman, T. A., Dammerman, R. S. & Kriegstein, A. R. Neurons derived from radial glial cells establish radial units in neocortex. *Nature* **409**, 714-720, doi:10.1038/35055553 (2001).

73 Coutinho, P. *et al.* Discovery and assessment of conserved Pax6 target genes and enhancers. *Genome Res* **21**, 1349-1359, doi:10.1101/gr.124115.111 (2011).

74 Visel, A. *et al.* Regulatory pathway analysis by high-throughput in situ hybridization. *PLoS Genet* **3**, 1867-1883, doi:10.1371/journal.pgen.0030178 (2007).

75 Cho, I. T., Lim, Y., Golden, J. A. & Cho, G. Aristaless Related Homeobox (ARX) Interacts with beta-Catenin, BCL9, and P300 to Regulate Canonical Wnt Signaling. *PLoS One* **12**, e0170282, doi:10.1371/journal.pone.0170282 (2017).

76 Esteve, P., Crespo, I., Kaimakis, P., Sandonis, A. & Bovolenta, P. Sfrp1 Modulates Cell-signaling Events Underlying Telencephalic Patterning, Growth and Differentiation. *Cereb Cortex* **29**, 1059-1074, doi:10.1093/cercor/bhy013 (2019).

77 Donega, V. *et al.* Single-cell profiling of human subventricular zone progenitors identifies SFRP1 as a target to re-activate progenitors. *Nat Commun* **13**, 1036, doi:10.1038/s41467-022-28626-9 (2022).

78 Ferron, S. R. *et al.* Postnatal loss of Dlk1 imprinting in stem cells and niche astrocytes regulates neurogenesis. *Nature* **475**, 381-385, doi:10.1038/nature10229 (2011).

79 Okazaki, S. *et al.* Aristaless-related homeobox gene disruption leads to abnormal distribution of GABAergic interneurons in human neocortex: evidence based on a case of X-linked lissencephaly with abnormal genitalia (XLAG). *Acta Neuropathol* **116**, 453-462, doi:10.1007/s00401-008-0382-2 (2008).

80 Griffin, A. *et al.* Phenotypic analysis of catastrophic childhood epilepsy genes. *Communications Biology* **4**, doi:10.1038/s42003-021-02221-y (2021).

81 Bortone, D. & Polleux, F. KCC2 expression promotes the termination of cortical interneuron migration in a voltage-sensitive calcium-dependent manner. *Neuron* **62**, 53-71, doi:10.1016/j.neuron.2009.01.034 (2009).

82 Lysko, D. E., Putt, M. & Golden, J. A. SDF1 regulates leading process branching and speed of migrating interneurons. *J Neurosci* **31**, 1739-1745, doi:10.1523/JNEUROSCI.3118-10.2011 (2011).

83 Colasante, G. *et al.* Arx acts as a regional key selector gene in the ventral telencephalon mainly through its transcriptional repression activity. *Dev Biol* **334**, 59-71, doi:10.1016/j.ydbio.2009.07.014 (2009).

84 Cossee, M. *et al.* ARX polyalanine expansions are highly implicated in familial cases of mental retardation with infantile epilepsy and/or hand dystonia. *Am J Med Genet A* **155A**, 98-105, doi:10.1002/ajmg.a.33785 (2011).

85 Kato, M., Koyama, N., Ohta, M., Miura, K. & Hayasaka, K. Frameshift mutations of the ARX gene in familial Ohtahara syndrome. *Epilepsia* **51**, 1679-1684, doi:10.1111/j.1528-1167.2010.02559.x (2010).

86 Trujillo, C. A. *et al.* Complex Oscillatory Waves Emerging from Cortical Organoids Model Early Human Brain Network Development. *Cell Stem Cell*, doi:10.1016/j.stem.2019.08.002 (2019).

87 Jiruska, P. *et al.* Synchronization and desynchronization in epilepsy: controversies and hypotheses. *J Physiol* **591**, 787-797, doi:10.1113/jphysiol.2012.239590 (2013).

88 van van Hugte, E. J. H., Schubert, D. & Nadif Kasri, N. Excitatory/inhibitory balance in epilepsies and neurodevelopmental disorders: Depolarizing gamma-aminobutyric acid as a common mechanism. *Epilepsia* **64**, 1975-1990, doi:10.1111/epi.17651 (2023).

89 Kasyanov, A. M., Safiulina, V. F., Voronin, L. L. & Cherubini, E. GABA-mediated giant depolarizing potentials as coincidence detectors for enhancing synaptic efficacy in the developing hippocampus. *Proc Natl Acad Sci U S A* **101**, 3967-3972, doi:10.1073/pnas.0305974101 (2004).

90 Ben-Ari, Y., Gaiarsa, J. L., Tyzio, R. & Khazipov, R. GABA: a pioneer transmitter that excites immature neurons and generates primitive oscillations. *Physiol Rev* **87**, 1215-1284, doi:10.1152/physrev.00017.2006 (2007).

91 Rosa, F. *et al.* In Vitro Differentiated Human Stem Cell-Derived Neurons Reproduce Synaptic Synchronicity Arising during Neurodevelopment. *Stem Cell Reports* **15**, 22-37, doi:10.1016/j.stemcr.2020.05.015 (2020).

92 Mirsadeghi, S. & Kiani, S. Voltage and ligand-gated ion channels appearance and function in neurodevelopment. *Factors Affect. Neurodev.*, 321–333, doi:doi:10.1016/b978-0-12-817986-4.00028-6 (2021).

93 Haider, B., Duque, A., Hasenstaub, A. R. & McCormick, D. A. Neocortical network activity in vivo is generated through a dynamic balance of excitation and inhibition. *J Neurosci* **26**, 4535-4545, doi:10.1523/JNEUROSCI.5297-05.2006 (2006).

94 Guerrini, R. *et al.* Developmental and epileptic encephalopathies: from genetic heterogeneity to phenotypic continuum. *Physiol Rev* **103**, 433-513, doi:10.1152/physrev.00063.2021 (2023).

95 Represa, A. Why Malformations of Cortical Development Cause Epilepsy. *Front Neurosci* **13**, 250, doi:10.3389/fnins.2019.00250 (2019).

96 Skalny, A., Chernova, L. & Skalnaya, A. Essential trace elements in neurodevelopment: An updated narrative. . *Vitamins and Minerals in Neurological Disorders* **Elsevier Inc.**, doi:doi:10.1016/B978-0-323-89835-5.00033-8. (2023).

97 Ben-Ari, Y. Excitatory actions of gaba during development: the nature of the nurture. *Nat Rev Neurosci* **3**, 728-739, doi:10.1038/nrn920 (2002).

98 Magloire, V., Cornford, J., Lieb, A., Kullmann, D. M. & Pavlov, I. KCC2 overexpression prevents the paradoxical seizure-promoting action of somatic inhibition. *Nat Commun* **10**, 1225, doi:10.1038/s41467-019-08933-4 (2019).

99 Peng, Z. *et al.* A reorganized GABAergic circuit in a model of epilepsy: evidence from optogenetic labeling and stimulation of somatostatin interneurons. *J Neurosci* **33**, 14392-14405, doi:10.1523/JNEUROSCI.2045-13.2013 (2013).

100 Galanopoulou, A. S. GABA(A) receptors in normal development and seizures: friends or foes? *Curr Neuropharmacol* **6**, 1-20, doi:10.2174/157015908783769653 (2008).

101 Olivetti, P. R., Maheshwari, A. & Noebels, J. L. Neonatal estradiol stimulation prevents epilepsy in Arx model of X-linked infantile spasms syndrome. *Sci Transl Med* **6**, 220ra212, doi:10.1126/scitranslmed.3007231 (2014).

102 Hao, Y. *et al.* Integrated analysis of multimodal single-cell data. *Cell* **184**, 3573-3587 e3529, doi:10.1016/j.cell.2021.04.048 (2021).

103 Stuart, T. *et al.* Comprehensive Integration of Single-Cell Data. *Cell* **177**, 1888-1902 e1821, doi:10.1016/j.cell.2019.05.031 (2019).

104 Paulsen, B. *et al.* Autism genes converge on asynchronous development of shared neuron classes. *Nature* **602**, 268-273, doi:10.1038/s41586-021-04358-6 (2022).

105 Szücs, A. NeuroExpress program for analyzing patch-clamp data. *ResearchGate* (2022).

106 Mahmud, M., Pulizzi, R., Vasilaki, E. & Giugliano, M. QSpike tools: a generic framework for parallel batch preprocessing of extracellular neuronal signals recorded by substrate microelectrode arrays. *Front Neuroinform* **8**, 26, doi:10.3389/fninf.2014.00026 (2014).

107 Quiroga, R. Q., Nadasdy, Z. & Ben-Shaul, Y. Unsupervised spike detection and sorting with wavelets and superparamagnetic clustering. *Neural Comput* **16**, 1661-1687, doi:10.1162/089976604774201631 (2004).

108 Knox, C. K. Detection of neuronal interactions using correlation analysis. *Trends in Neurosciences* **Volume 4**, Pages 222-225, doi:https://doi.org/10.1016/0166-2236(81)90070-9 (1981).

Figure 1

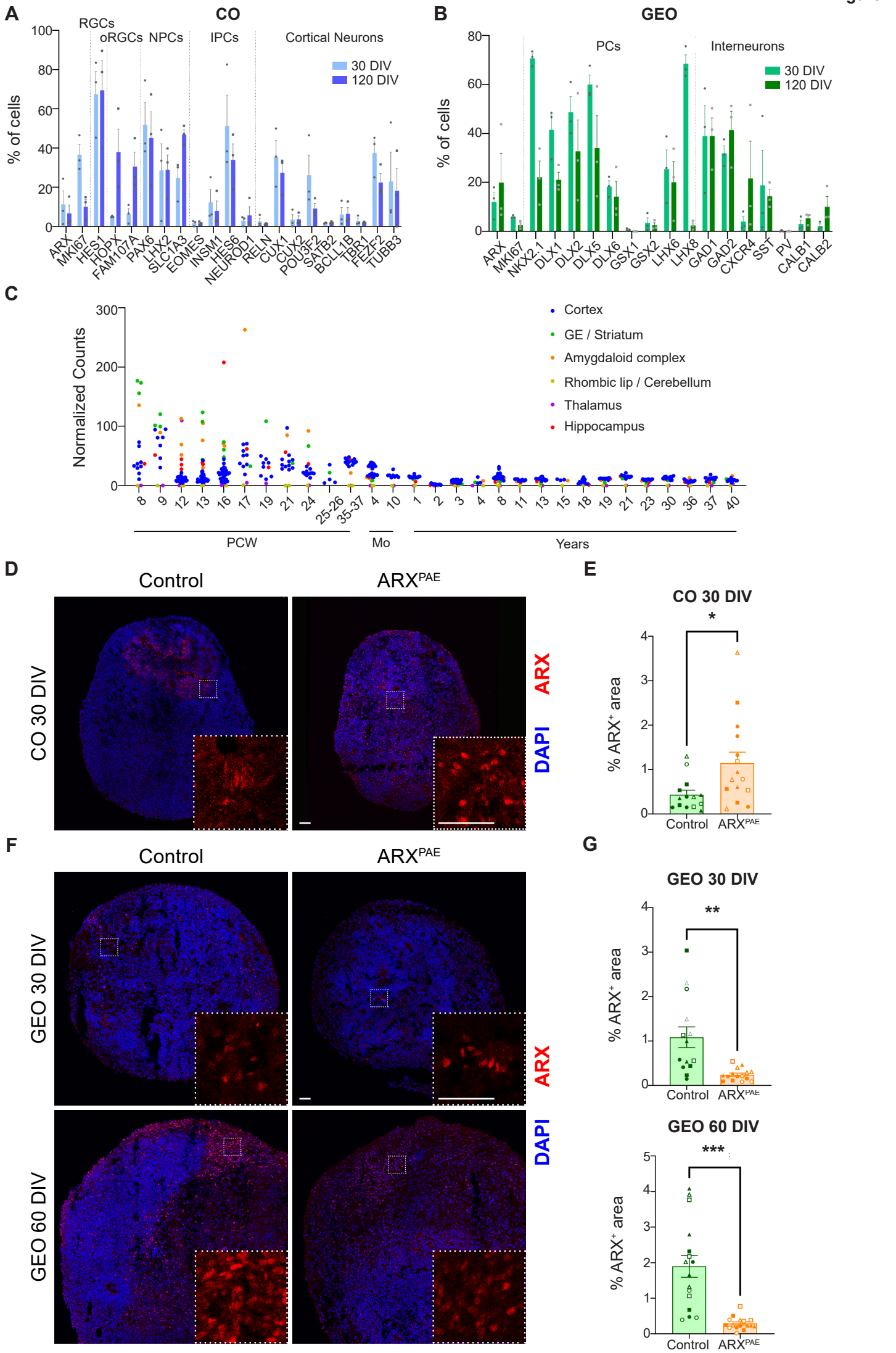
A
CO
RGCs
oRGCs
NPCs
IPCs
Cortical Neurons
30 DIV
120 DIV
% of cells
ARX
MKI67
HES1
HOPX
FAM107A
PAX6
LHX2
SLC1A3
EOMES
INSM1
HES6
NEUROD1
RELN
CUX1
CUX2
POU3F2
SATB2
BCL11B
TBR1
FEZF2
TUBB3
B
GEO
PCs
Interneurons
30 DIV
120 DIV
% of cells
ARX
MKI67
NKX2.1
DLX1
DLX2
DLX5
DLX6
GSX1
GSX2
LHX6
LHX8
GAD1
GAD2
CXCR4
SST
PV
CALB1
CALB2
C
Normalized Counts
Cortex
GE / Striatum
Amygdaloid complex
Rhombic lip / Cerebellum
Thalamus
Hippocampus
PCW
Mo
Years
D
Control
ARX^PAE
CO 30 DIV
ARX
DAPI
E
CO 30 DIV
% ARX+ area
Control
ARX^PAE
F
Control
ARX^PAE
GEO 30 DIV
GEO 60 DIV
ARX
DAPI
G
GEO 30 DIV
GEO 60 DIV
% ARX+ area
Control
ARX^PAE

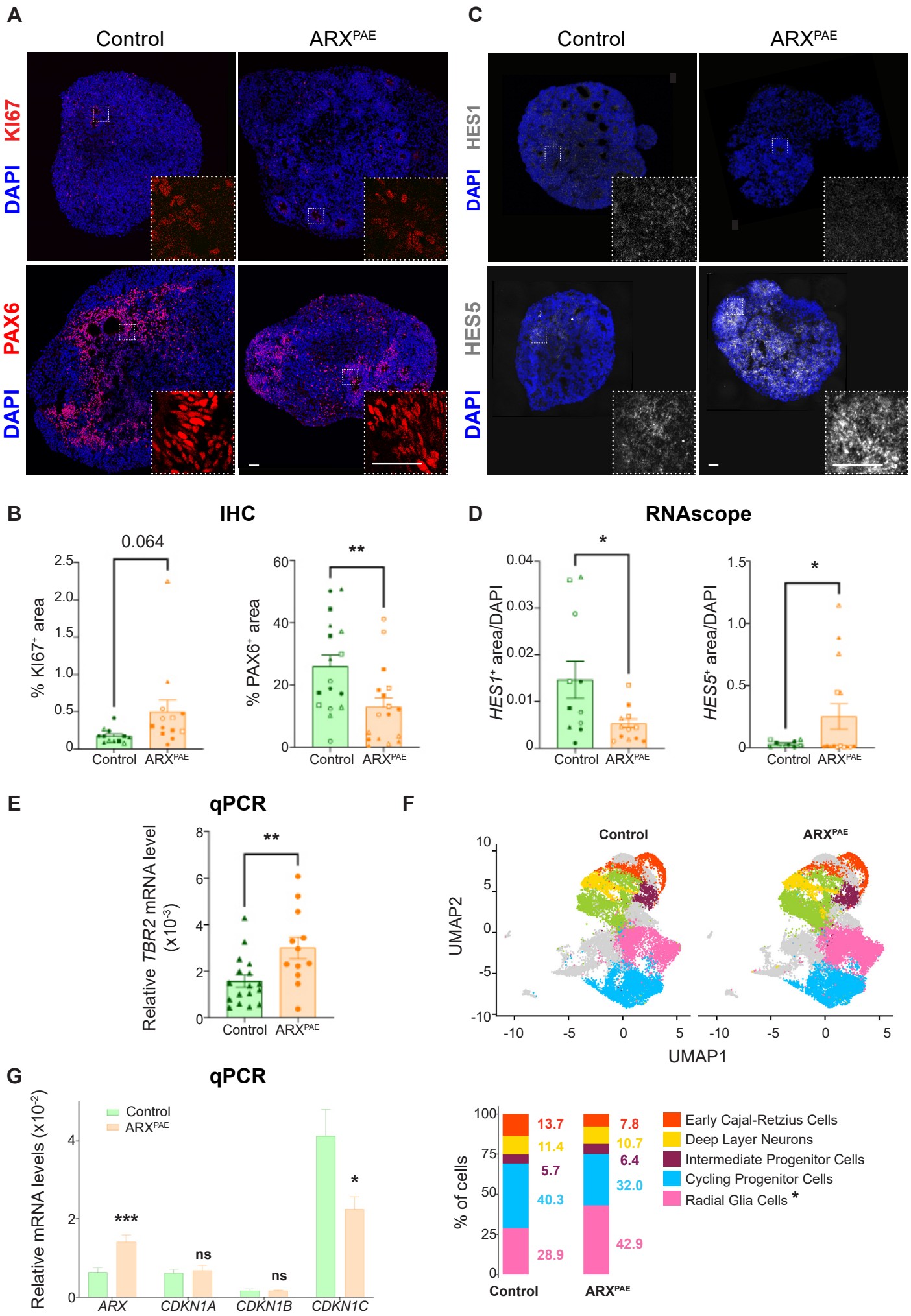
A
Control
ARXPAE
KI67
DAPI
PAX6
DAPI
C
Control
ARXPAE
HES1
DAPI
HES5
DAPI
B
IHC
0.064
% KI67+ area
Control
ARXPAE
**
% PAX6+ area
Control
ARXPAE
D
RNAscope
*
HES1+ area/DAPI
Control
ARXPAE
*
HES5+ area/DAPI
Control
ARXPAE
E
qPCR
**
Relative TBR2 mRNA level (x10-3)
Control
ARXPAE
F
Control
ARXPAE
UMAP2
UMAP1
G
qPCR
Control
ARXPAE
Relative mRNA levels (x10-2)
***
ns
ns
*
ARX
CDKN1A
CDKN1B
CDKN1C
% of cells
13.7
11.4
5.7
40.3
28.9
7.8
10.7
6.4
32.0
42.9
Control
ARXPAE
Early Cajal-Retzius Cells
Deep Layer Neurons
Intermediate Progenitor Cells
Cycling Progenitor Cells
Radial Glia Cells *

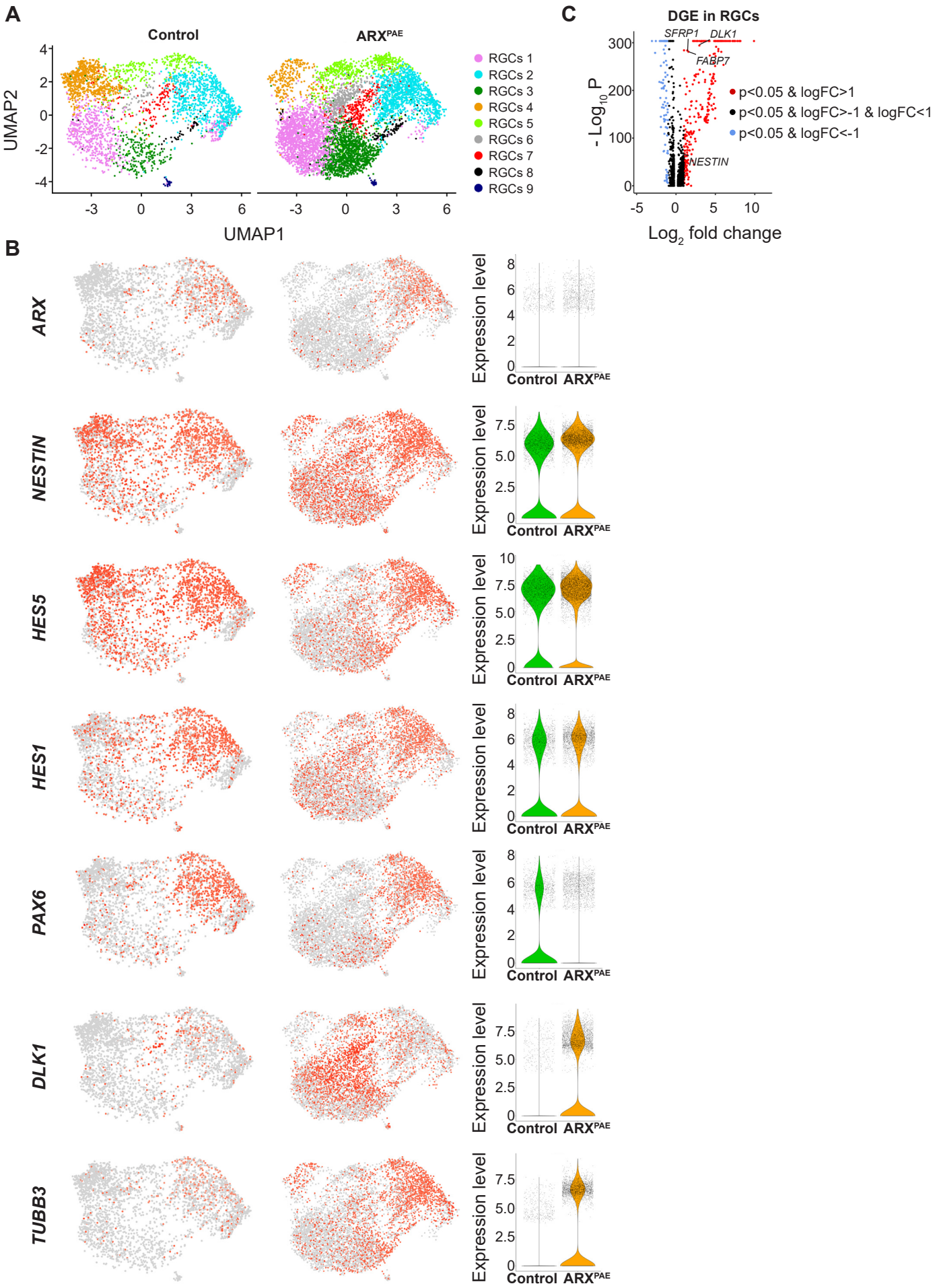
A
Control
ARXPAE
UMAP2
UMAP1
RGCs 1
RGCs 2
RGCs 3
RGCs 4
RGCs 5
RGCs 6
RGCs 7
RGCs 8
RGCs 9
C
DGE in RGCs
SFRP1
DLK1
FABP7
NESTIN
- Log10 P
Log2 fold change
p<0.05 & logFC>1
p<0.05 & logFC>-1 & logFC<1
p<0.05 & logFC<-1
B
ARX
NESTIN
HES5
HES1
PAX6
DLK1
TUBB3
Expression level
Control
ARXPAE

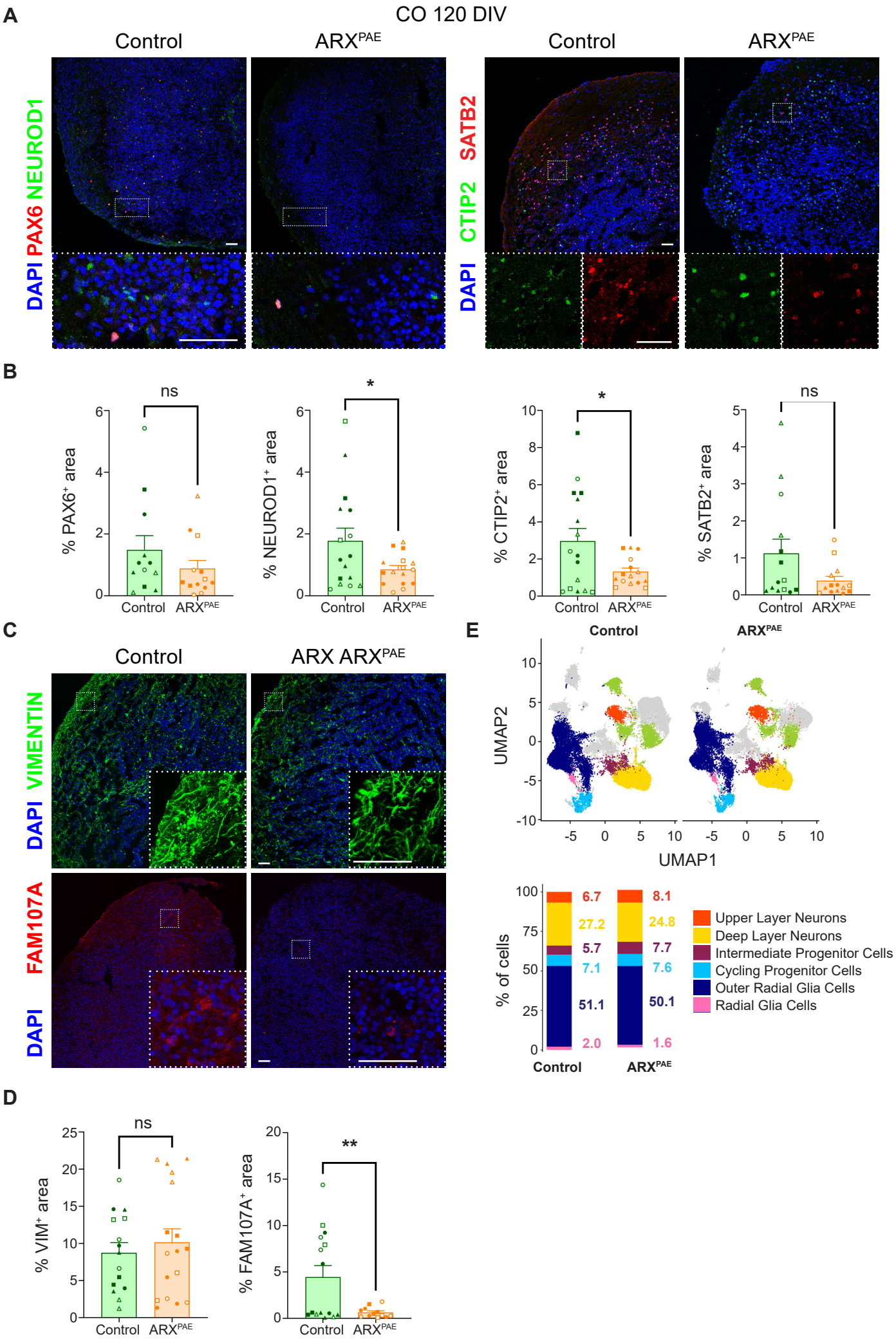
A
CO 120 DIV
Control
ARXPAE
Control
ARXPAE
DAPI PAX6 NEUROD1
DAPI CTIP2 SATB2
B
ns
*
*
ns
% PAX6+ area
% NEUROD1+ area
% CTIP2+ area
% SATB2+ area
Control
ARXPAE
C
Control
ARX ARXPAE
DAPI VIMENTIN
DAPI FAM107A
D
ns
**
% VIM+ area
% FAM107A+ area
E
Control
ARXPAE
UMAP2
UMAP1
% of cells
6.7
27.2
5.7
7.1
51.1
2.0
8.1
24.8
7.7
7.6
50.1
1.6
Upper Layer Neurons
Deep Layer Neurons
Intermediate Progenitor Cells
Cycling Progenitor Cells
Outer Radial Glia Cells
Radial Glia Cells

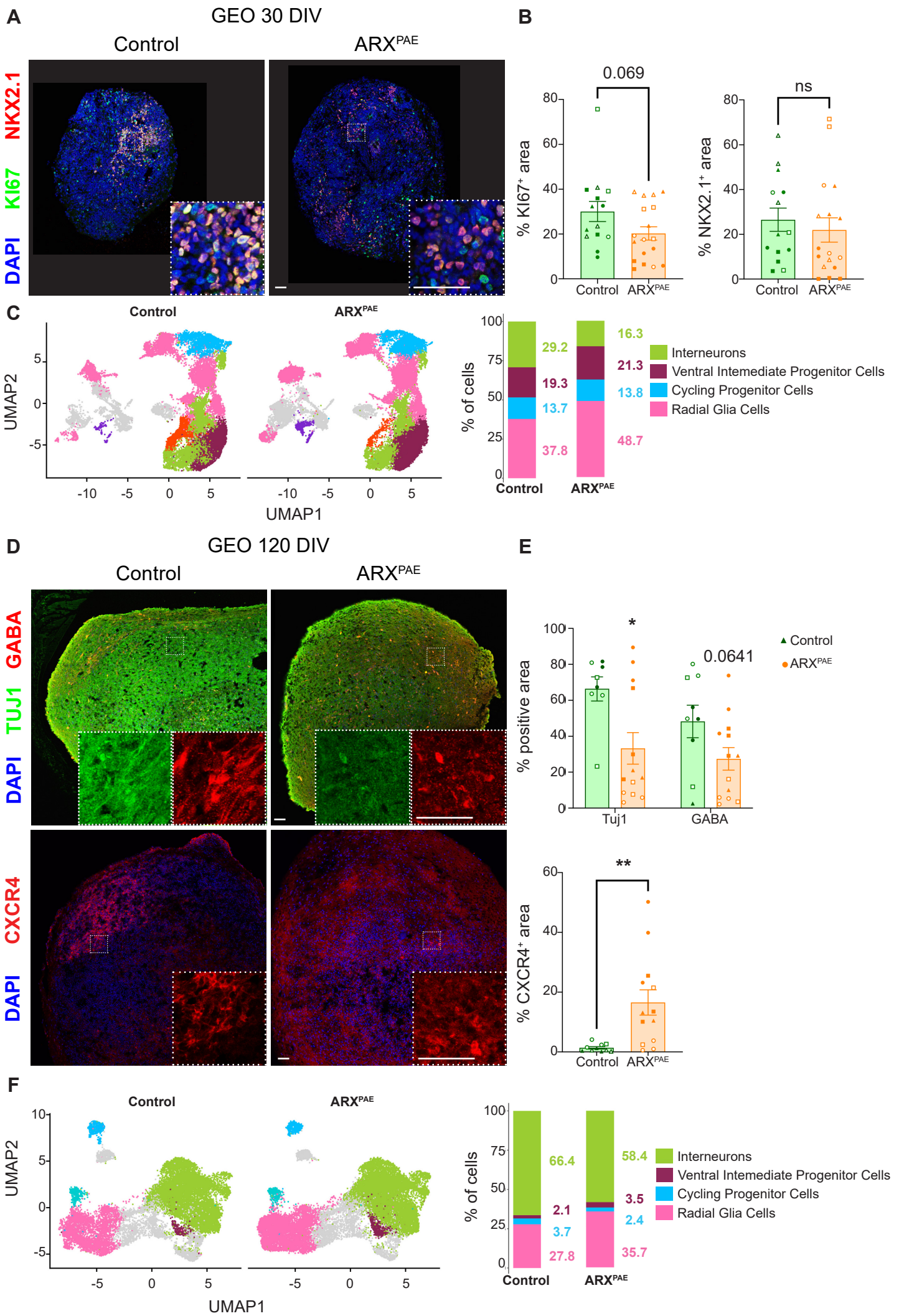
A
GEO 30 DIV
Control
ARXPAE
NKX2.1
KI67
DAPI
B
0.069
% KI67+ area
Control
ARXPAE
ns
% NKX2.1+ area
C
Control
ARXPAE
UMAP2
UMAP1
% of cells
29.2
19.3
13.7
37.8
16.3
21.3
13.8
48.7
Interneurons
Ventral Intemediate Progenitor Cells
Cycling Progenitor Cells
Radial Glia Cells
D
GEO 120 DIV
Control
ARXPAE
GABA
TUJ1
DAPI
CXCR4
E
*
0.0641
% positive area
Tuj1
GABA
Control
ARXPAE
**
% CXCR4+ area
F
Control
ARXPAE
UMAP2
UMAP1
% of cells
66.4
2.1
3.7
27.8
58.4
3.5
2.4
35.7
Interneurons
Ventral Intemediate Progenitor Cells
Cycling Progenitor Cells
Radial Glia Cells

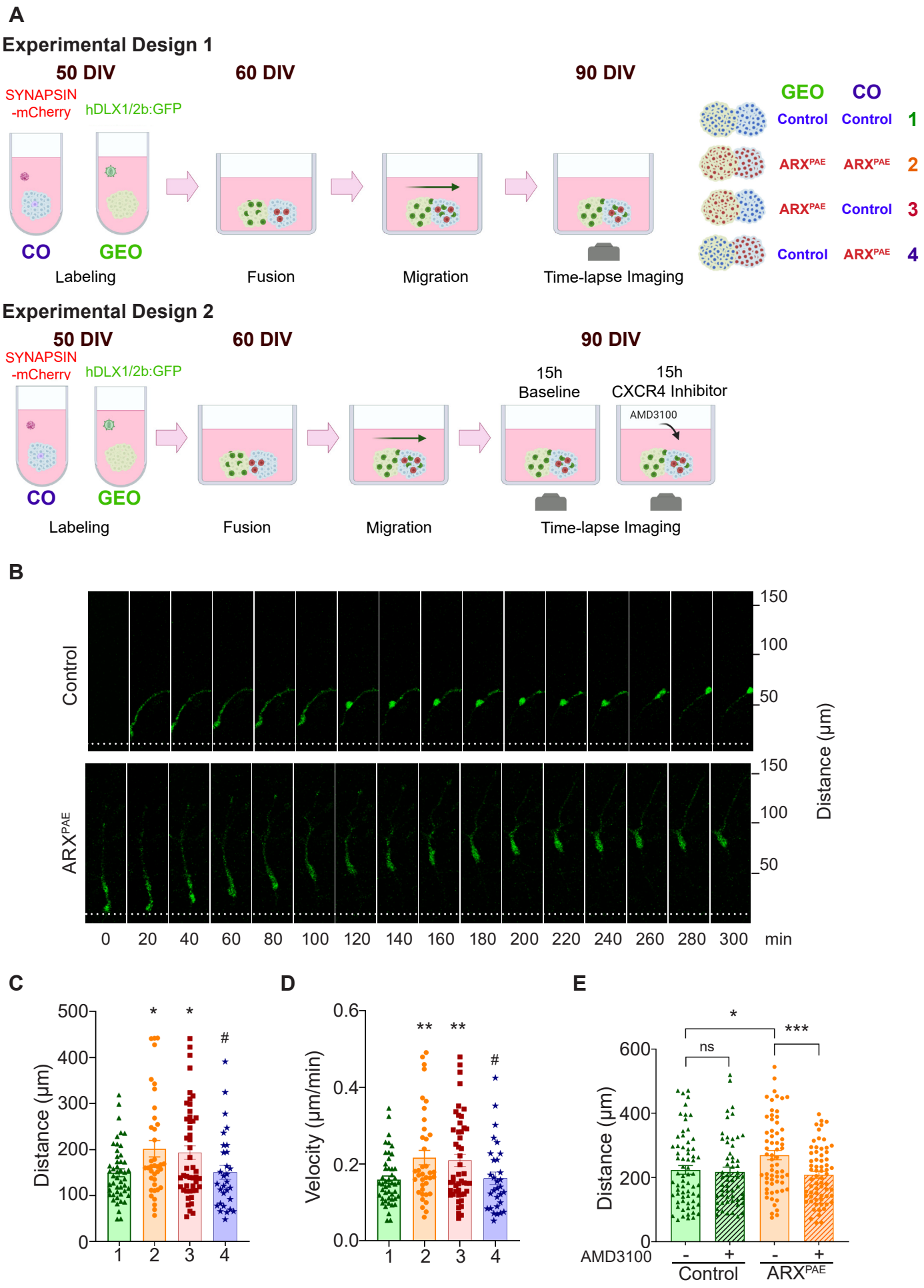
A
Experimental Design 1
50 DIV
60 DIV
90 DIV
SYNAPSIN -mCherry
hDLX1/2b:GFP
CO
GEO
Labeling
Fusion
Migration
Time-lapse Imaging
GEO
CO
Control
Control
1
ARXPAE
ARXPAE
2
ARXPAE
Control
3
Control
ARXPAE
4
Experimental Design 2
50 DIV
60 DIV
90 DIV
SYNAPSIN -mCherry
hDLX1/2b:GFP
15h Baseline
15h CXCR4 Inhibitor
AMD3100
CO
GEO
Labeling
Fusion
Migration
Time-lapse Imaging
B
Control
ARXPAE
150
100
50
Distance (µm)
0
20
40
60
80
100
120
140
160
180
200
220
240
260
280
300
min
C
Distance (µm)
500
400
300
200
100
0
1
2
3
4
D
Velocity (µm/min)
0.6
0.4
0.2
0.0
E
Distance (µm)
600
400
200
0
ns
AMD3100
Control
ARXPAE

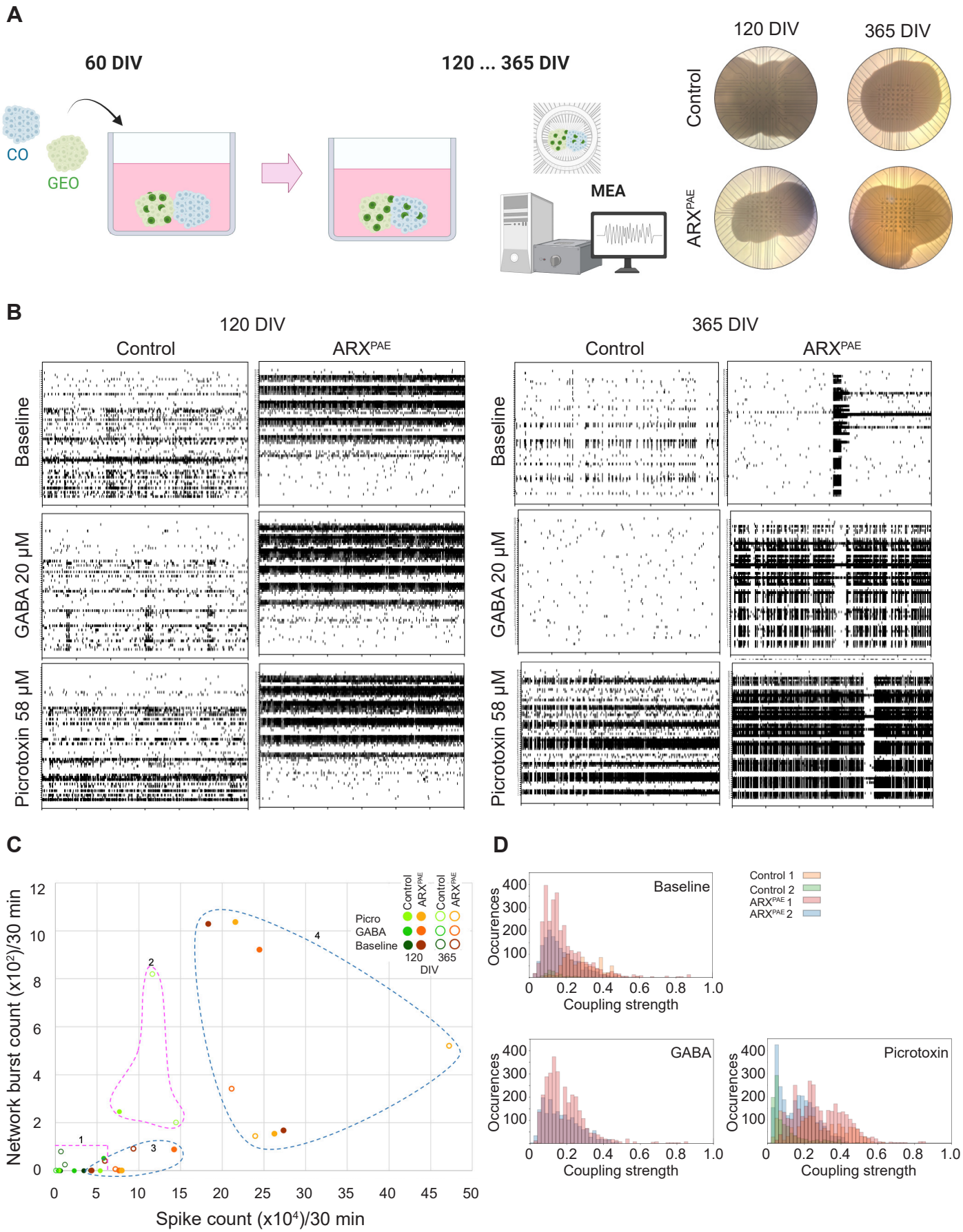
A
60 DIV
120 ... 365 DIV
CO
GEO
MEA
120 DIV
365 DIV
Control
ARXPAE
B
120 DIV
365 DIV
Control
ARXPAE
Baseline
GABA 20 µM
Picrotoxin 58 µM
C
Network burst count (x10²)/30 min
Spike count (x10⁴)/30 min
Picro
GABA
Baseline
Control
ARXPAE
120
365
DIV
D
Baseline
GABA
Picrotoxin
Occurences
Coupling strength
Control 1
Control 2
ARXPAE 1
ARXPAE 2

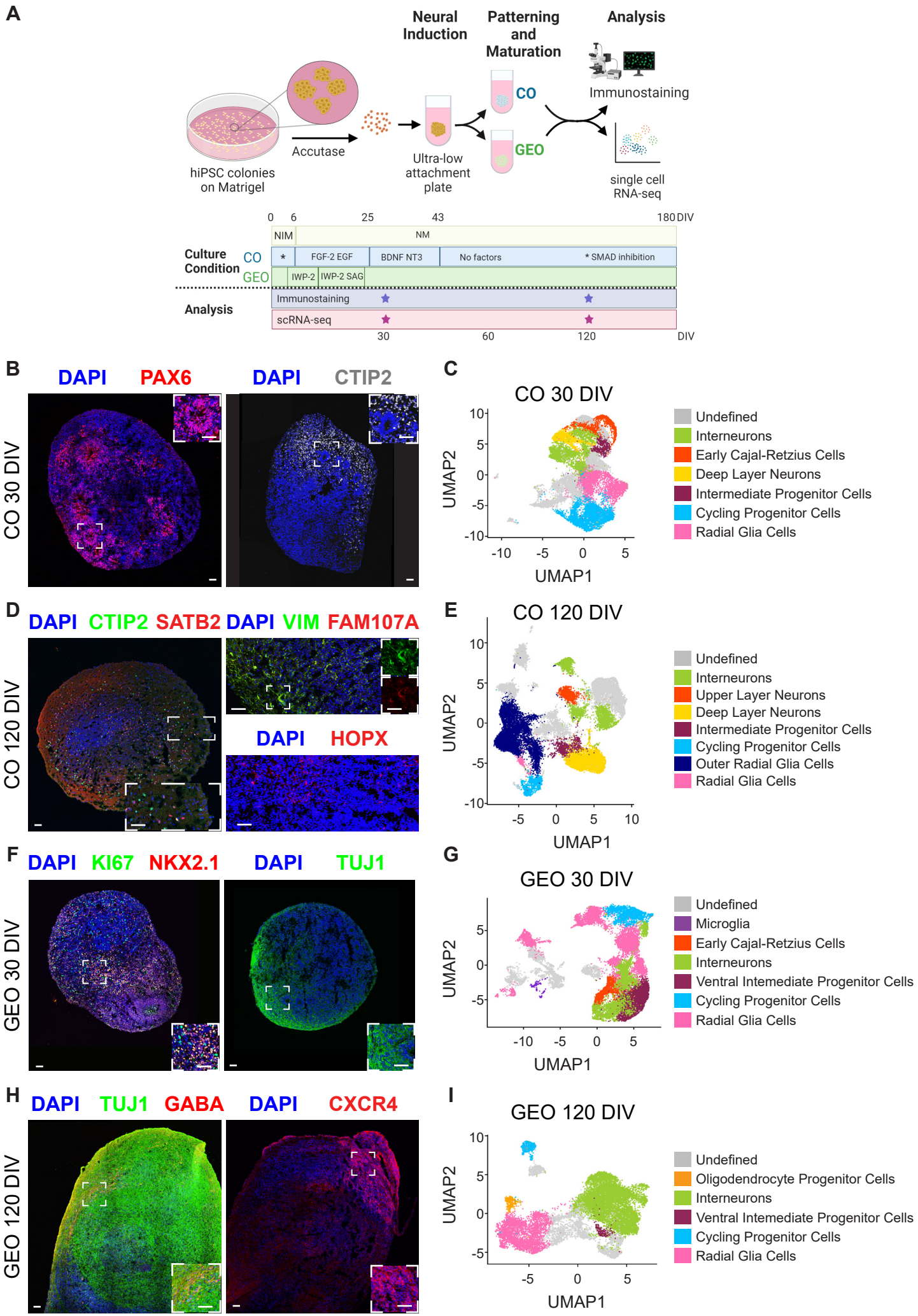
A
Neural Induction
Patterning and Maturation
Analysis
hiPSC colonies on Matrigel
Accutase
Ultra-low attachment plate
CO
GEO
Immunostaining
single cell RNA-seq
0 6 25 43 180 DIV
NIM
NM
Culture Condition
CO
GEO
FGF-2 EGF
BDNF NT3
No factors
* SMAD inhibition
IWP-2
IWP-2 SAG
Analysis
Immunostaining
scRNA-seq
30 60 120 DIV
B
DAPI PAX6
DAPI CTIP2
CO 30 DIV
C
CO 30 DIV
UMAP2
UMAP1
Undefined
Interneurons
Early Cajal-Retzius Cells
Deep Layer Neurons
Intermediate Progenitor Cells
Cycling Progenitor Cells
Radial Glia Cells
D
DAPI CTIP2 SATB2
DAPI VIM FAM107A
DAPI HOPX
CO 120 DIV
E
CO 120 DIV
UMAP2
UMAP1
Undefined
Interneurons
Upper Layer Neurons
Deep Layer Neurons
Intermediate Progenitor Cells
Cycling Progenitor Cells
Outer Radial Glia Cells
Radial Glia Cells
F
DAPI KI67 NKX2.1
DAPI TUJ1
GEO 30 DIV
G
GEO 30 DIV
UMAP2
UMAP1
Undefined
Microglia
Early Cajal-Retzius Cells
Interneurons
Ventral Intemediate Progenitor Cells
Cycling Progenitor Cells
Radial Glia Cells
H
DAPI TUJ1 GABA
DAPI CXCR4
GEO 120 DIV
I
GEO 120 DIV
UMAP2
UMAP1
Undefined
Oligodendrocyte Progenitor Cells
Interneurons
Ventral Intemediate Progenitor Cells
Cycling Progenitor Cells
Radial Glia Cells

Figure S2

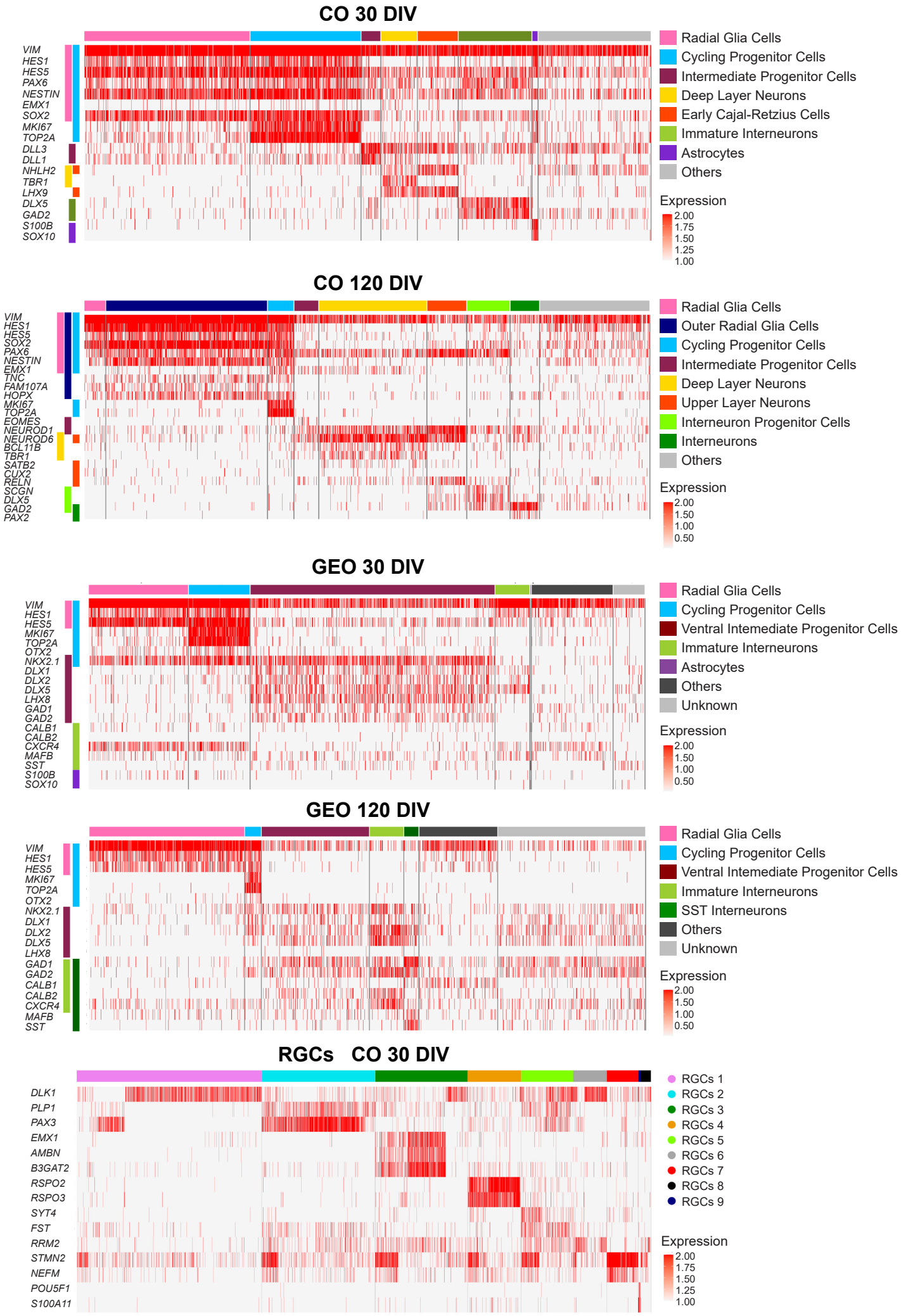
CO 30 DIV
VIM
HES1
HES5
PAX6
NESTIN
EMX1
SOX2
MKI67
TOP2A
DLL3
DLL1
NHLH2
TBR1
LHX9
DLX5
GAD2
S100B
SOX10
Radial Glia Cells
Cycling Progenitor Cells
Intermediate Progenitor Cells
Deep Layer Neurons
Early Cajal-Retzius Cells
Immature Interneurons
Astrocytes
Others
Expression
2.00
1.75
1.50
1.25
1.00
CO 120 DIV
VIM
HES1
HES5
SOX2
PAX6
NESTIN
EMX1
TNC
FAM107A
HOPX
MKI67
TOP2A
EOMES
NEUROD1
NEUROD6
BCL11B
TBR1
SATB2
CUX2
RELN
SCGN
DLX5
GAD2
PAX2
Radial Glia Cells
Outer Radial Glia Cells
Cycling Progenitor Cells
Intermediate Progenitor Cells
Deep Layer Neurons
Upper Layer Neurons
Interneuron Progenitor Cells
Interneurons
Others
Expression
2.00
1.50
1.00
0.50
GEO 30 DIV
VIM
HES1
HES5
MKI67
TOP2A
OTX2
NKX2.1
DLX1
DLX2
DLX5
LHX8
GAD1
GAD2
CALB1
CALB2
CXCR4
MAFB
SST
S100B
SOX10
Radial Glia Cells
Cycling Progenitor Cells
Ventral Intemediate Progenitor Cells
Immature Interneurons
Astrocytes
Others
Unknown
Expression
2.00
1.50
1.00
0.50
GEO 120 DIV
VIM
HES1
HES5
MKI67
TOP2A
OTX2
NKX2.1
DLX1
DLX2
DLX5
LHX8
GAD1
GAD2
CALB1
CALB2
CXCR4
MAFB
SST
Radial Glia Cells
Cycling Progenitor Cells
Ventral Intemediate Progenitor Cells
Immature Interneurons
SST Interneurons
Others
Unknown
Expression
2.00
1.50
1.00
0.50
RGCs CO 30 DIV
DLK1
PLP1
PAX3
EMX1
AMBN
B3GAT2
RSPO2
RSPO3
SYT4
FST
RRM2
STMN2
NEFM
POU5F1
S100A11
RGCs 1
RGCs 2
RGCs 3
RGCs 4
RGCs 5
RGCs 6
RGCs 7
RGCs 8
RGCs 9
Expression
2.00
1.75
1.50
1.25
1.00

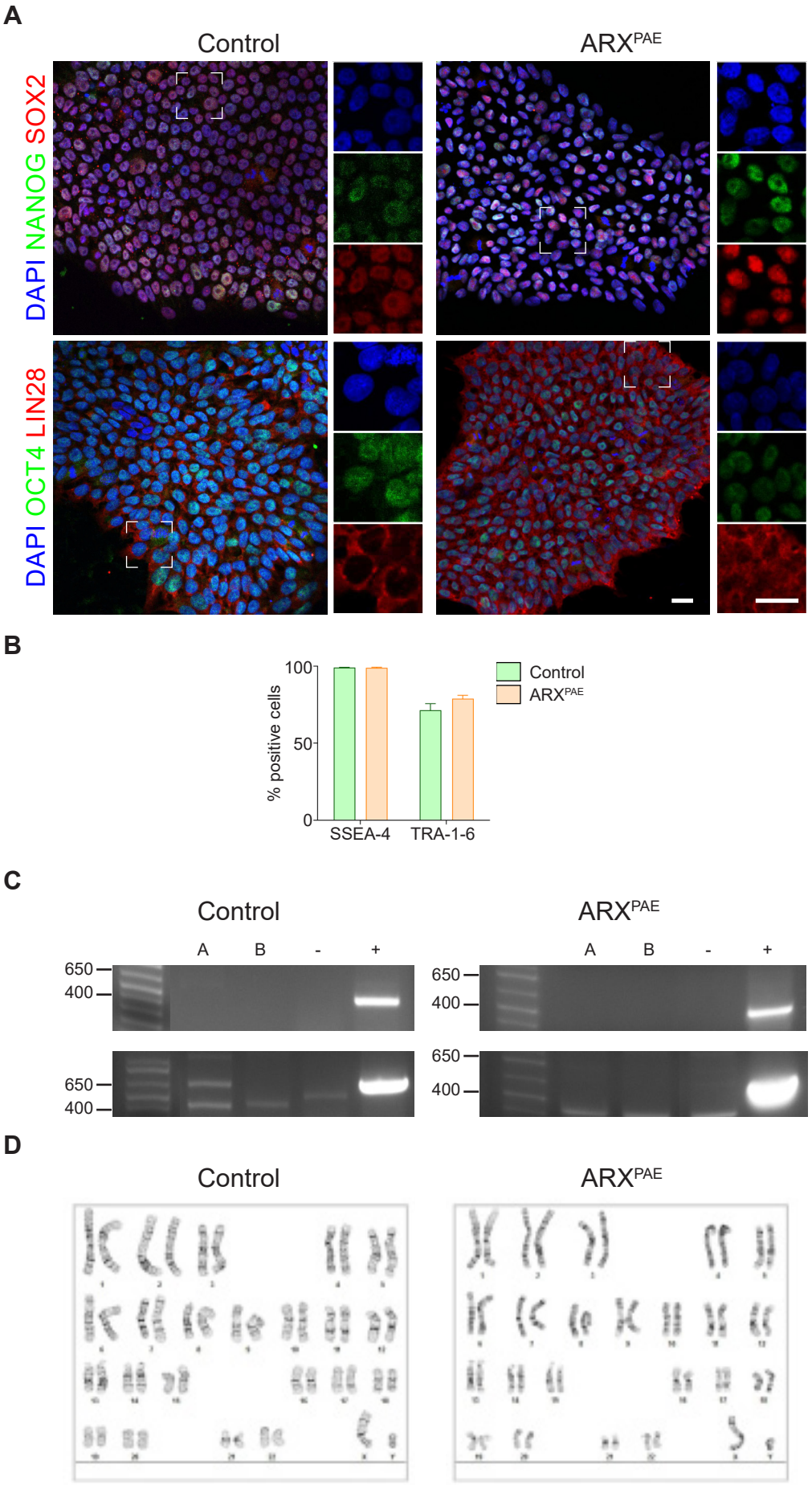
A
Control
ARXPAE
DAPI NANOG SOX2
DAPI OCT4 LIN28
B
% positive cells
100
50
0
SSEA-4
TRA-1-6
Control
ARXPAE
C
Control
ARXPAE
A
B
-
+
650
400
D
Control
ARXPAE

Figure S4

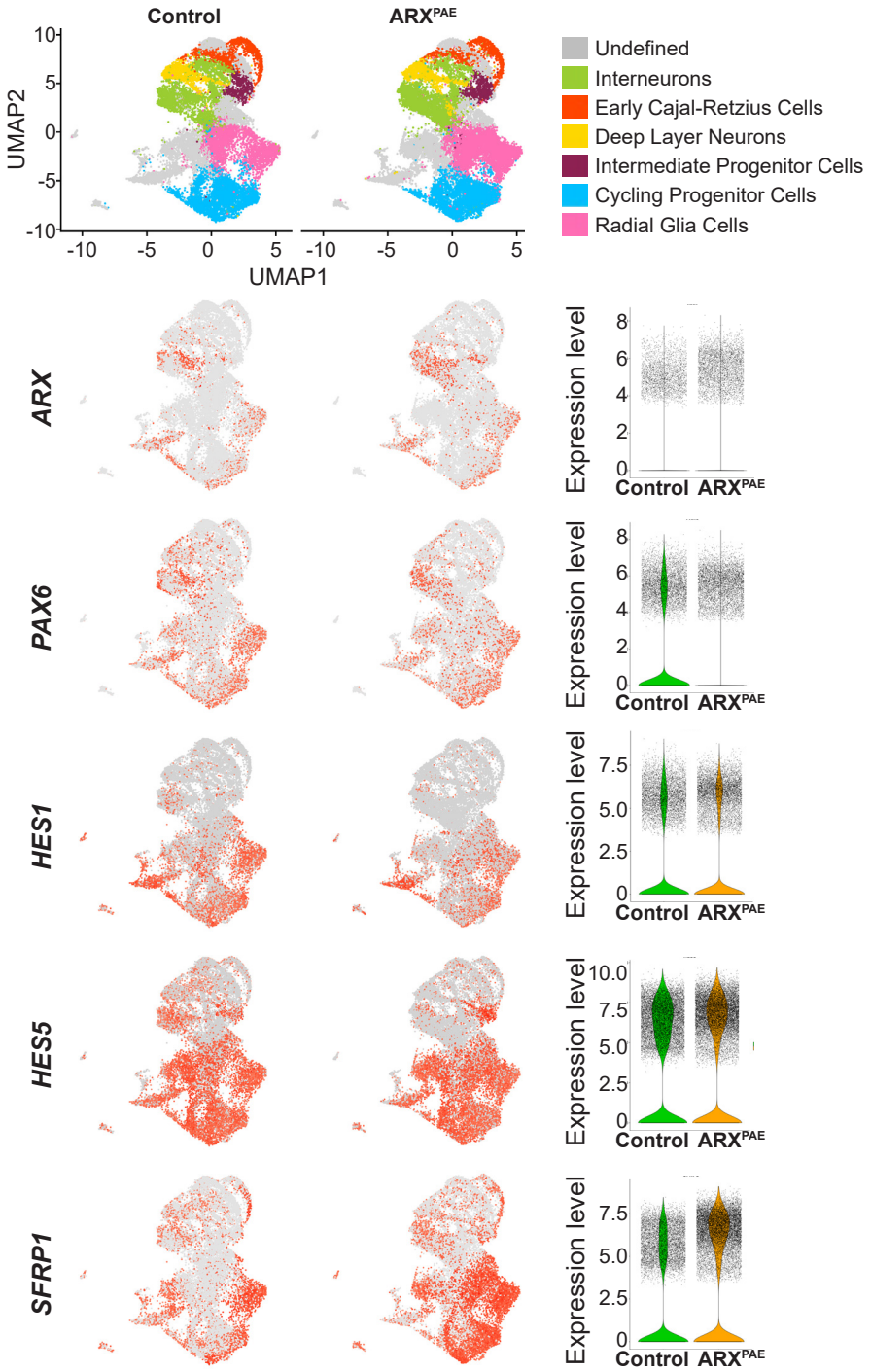
Control
ARXPAE
UMAP2
UMAP1
10
5
0
-5
-10
-10
-5
0
5
Undefined
Interneurons
Early Cajal-Retzius Cells
Deep Layer Neurons
Intermediate Progenitor Cells
Cycling Progenitor Cells
Radial Glia Cells
ARX
PAX6
HES1
HES5
SFRP1
Expression level
Control
ARXPAE

Figure S5

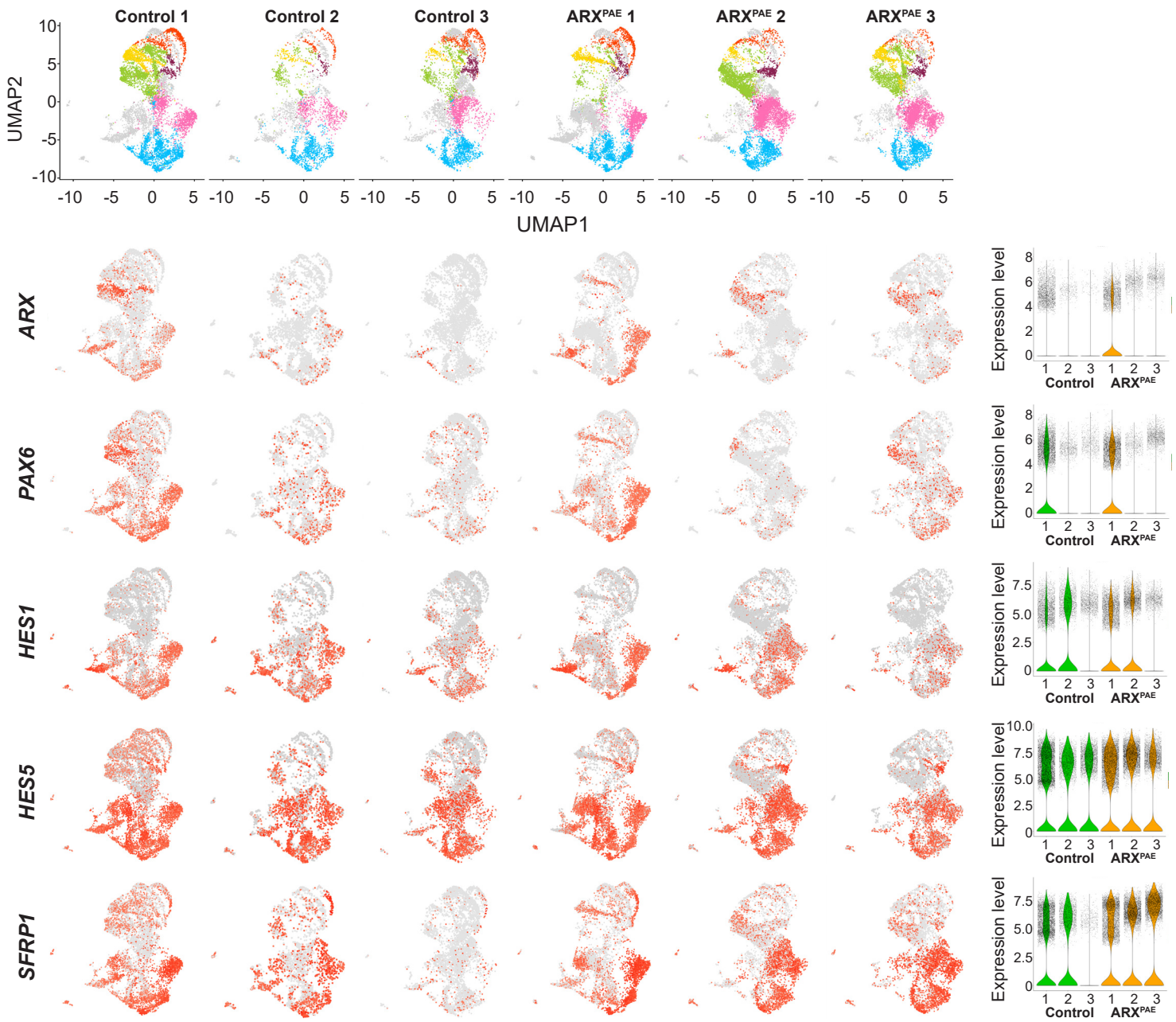
Control 1
Control 2
Control 3
ARXPAE 1
ARXPAE 2
ARXPAE 3
UMAP2
UMAP1
ARX
PAX6
HES1
HES5
SFRP1
Expression level
Control
ARXPAE

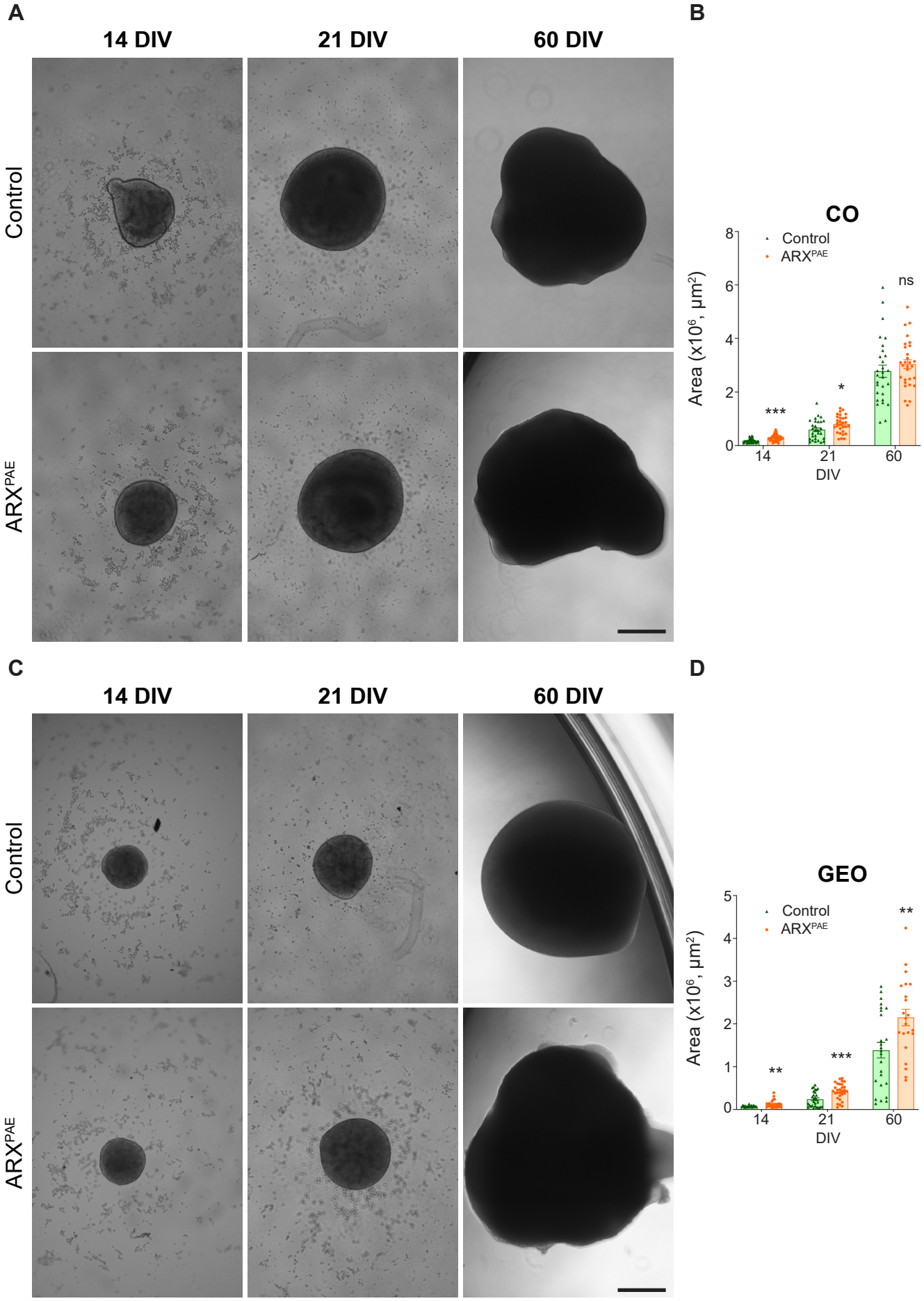
A
14 DIV
21 DIV
60 DIV
Control
ARXPAE
B
CO
Control
ARXPAE
Area (x10^6, µm^2)
8
6
4
2
0
***
*
ns
14
21
60
DIV
C
14 DIV
21 DIV
60 DIV
Control
ARXPAE
D
GEO
Control
ARXPAE
Area (x10^6, µm^2)
5
4
3
2
1
0
**
***
**
14
21
60
DIV

Figure S7

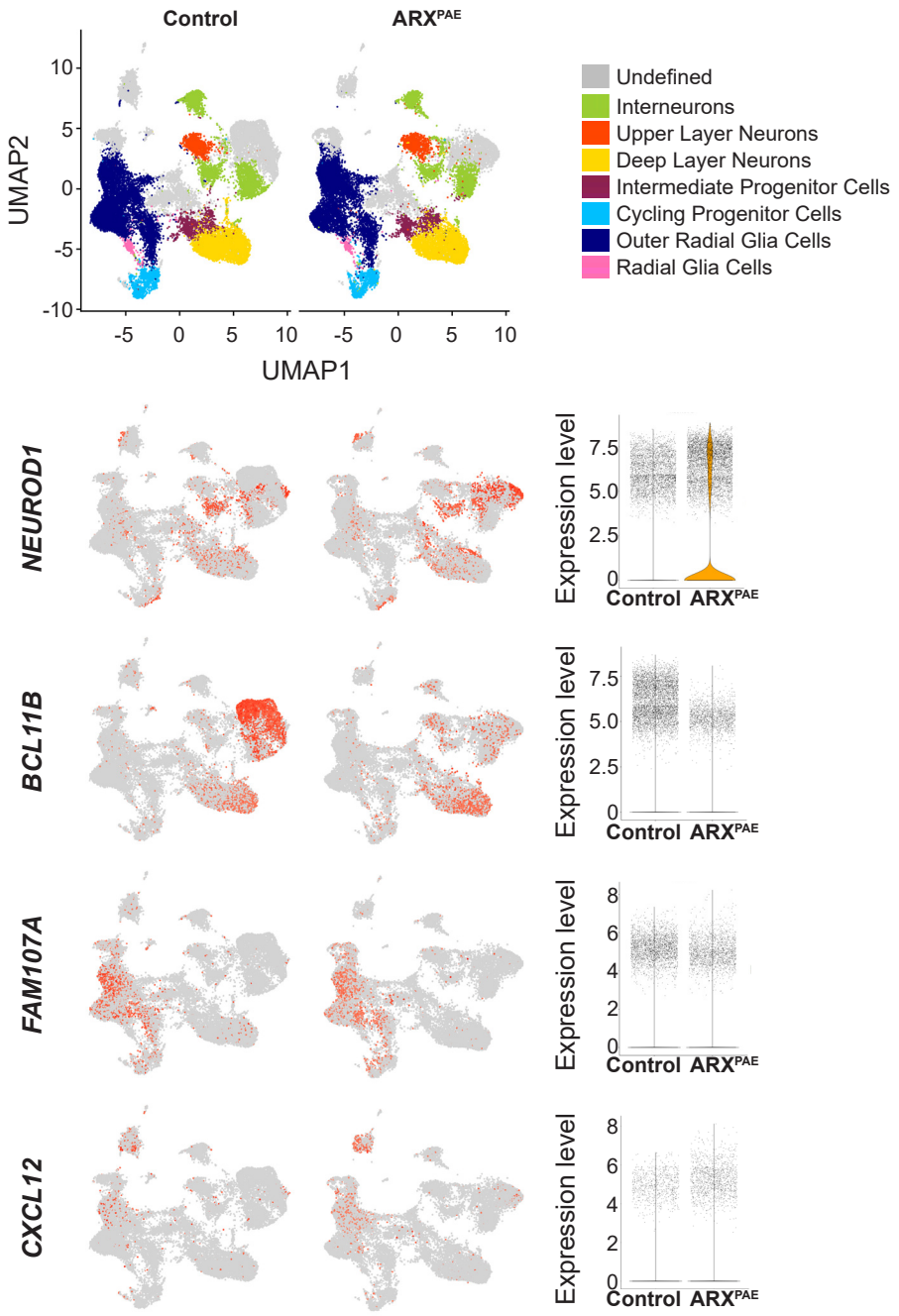
Control
ARXPAE
UMAP2
UMAP1
10
5
0
-5
-10
-5
0
5
10
Undefined
Interneurons
Upper Layer Neurons
Deep Layer Neurons
Intermediate Progenitor Cells
Cycling Progenitor Cells
Outer Radial Glia Cells
Radial Glia Cells
NEUROD1
BCL11B
FAM107A
CXCL12
Expression level
7.5
5.0
2.5
0
8
6
4
2
Control
ARXPAE

Figure S8

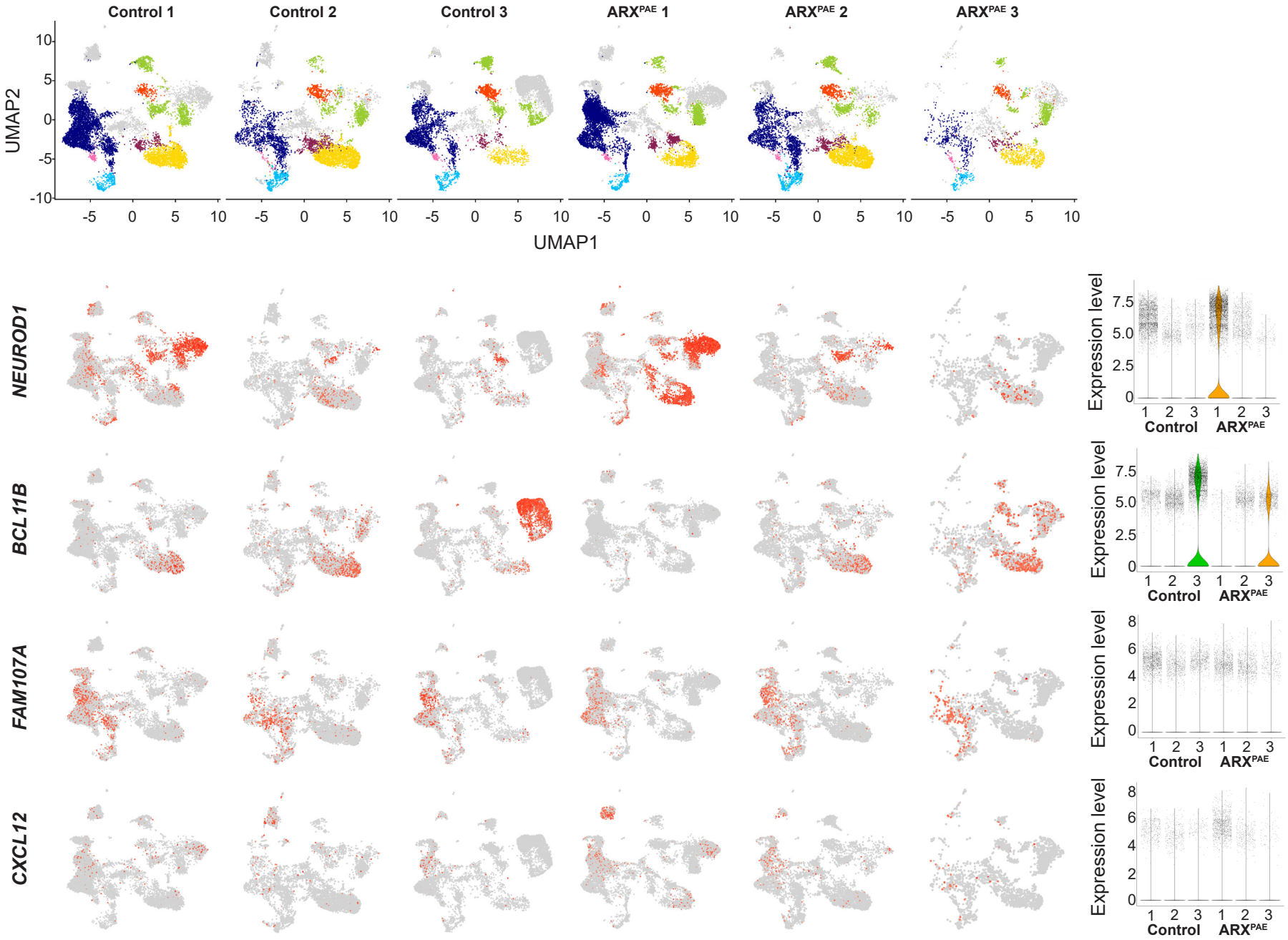
Control 1
Control 2
Control 3
ARX^PAE 1
ARX^PAE 2
ARX^PAE 3
UMAP2
UMAP1
NEUROD1
BCL11B
FAM107A
CXCL12
Expression level
Control
ARX^PAE

Figure S9

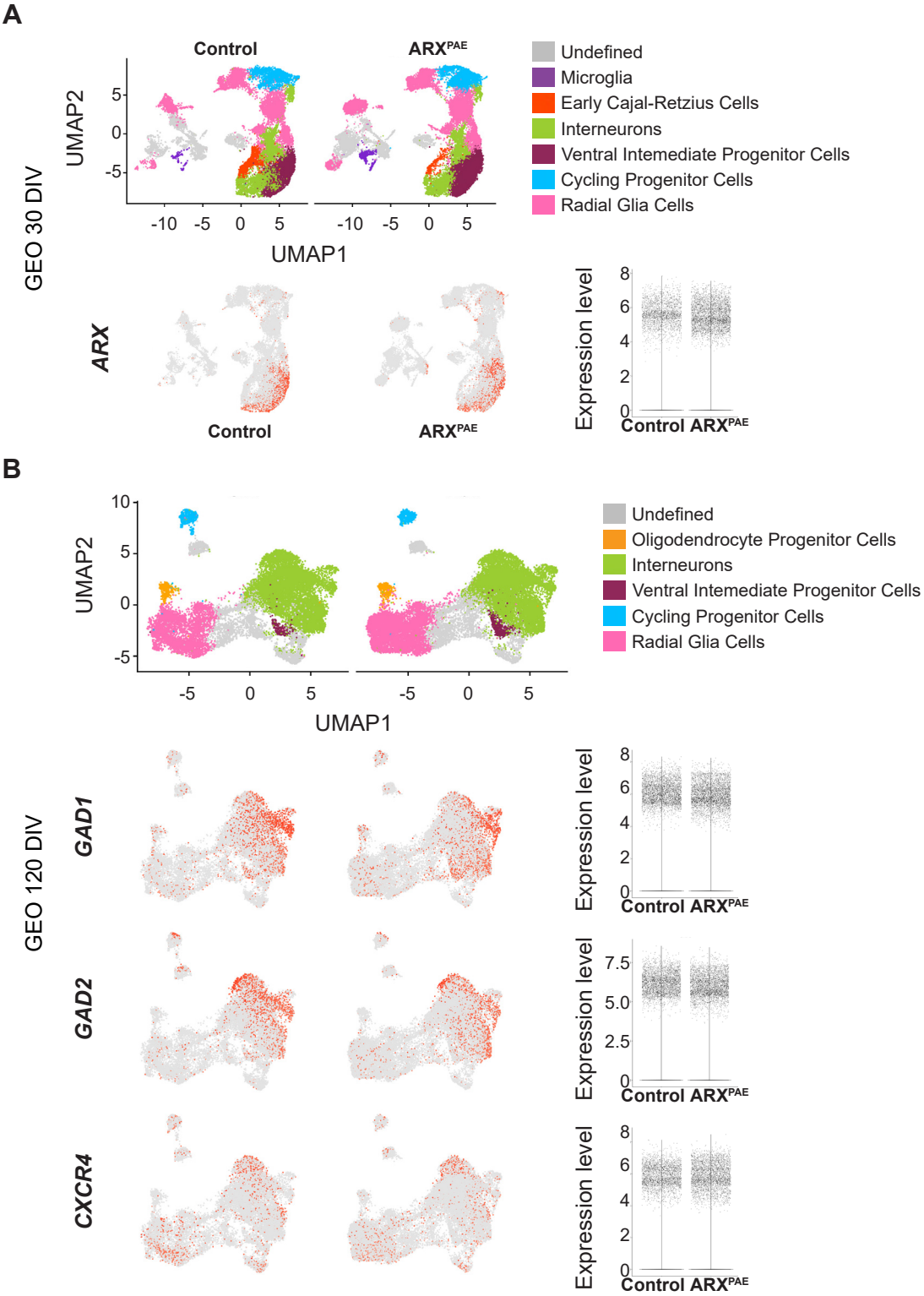
A
GEO 30 DIV
Control
ARXPAE
UMAP2
UMAP1
Undefined
Microglia
Early Cajal-Retzius Cells
Interneurons
Ventral Intemediate Progenitor Cells
Cycling Progenitor Cells
Radial Glia Cells
ARX
Expression level
Control ARXPAE
B
GEO 120 DIV
Undefined
Oligodendrocyte Progenitor Cells
Interneurons
Ventral Intemediate Progenitor Cells
Cycling Progenitor Cells
Radial Glia Cells
GAD1
GAD2
CXCR4

Figure S10

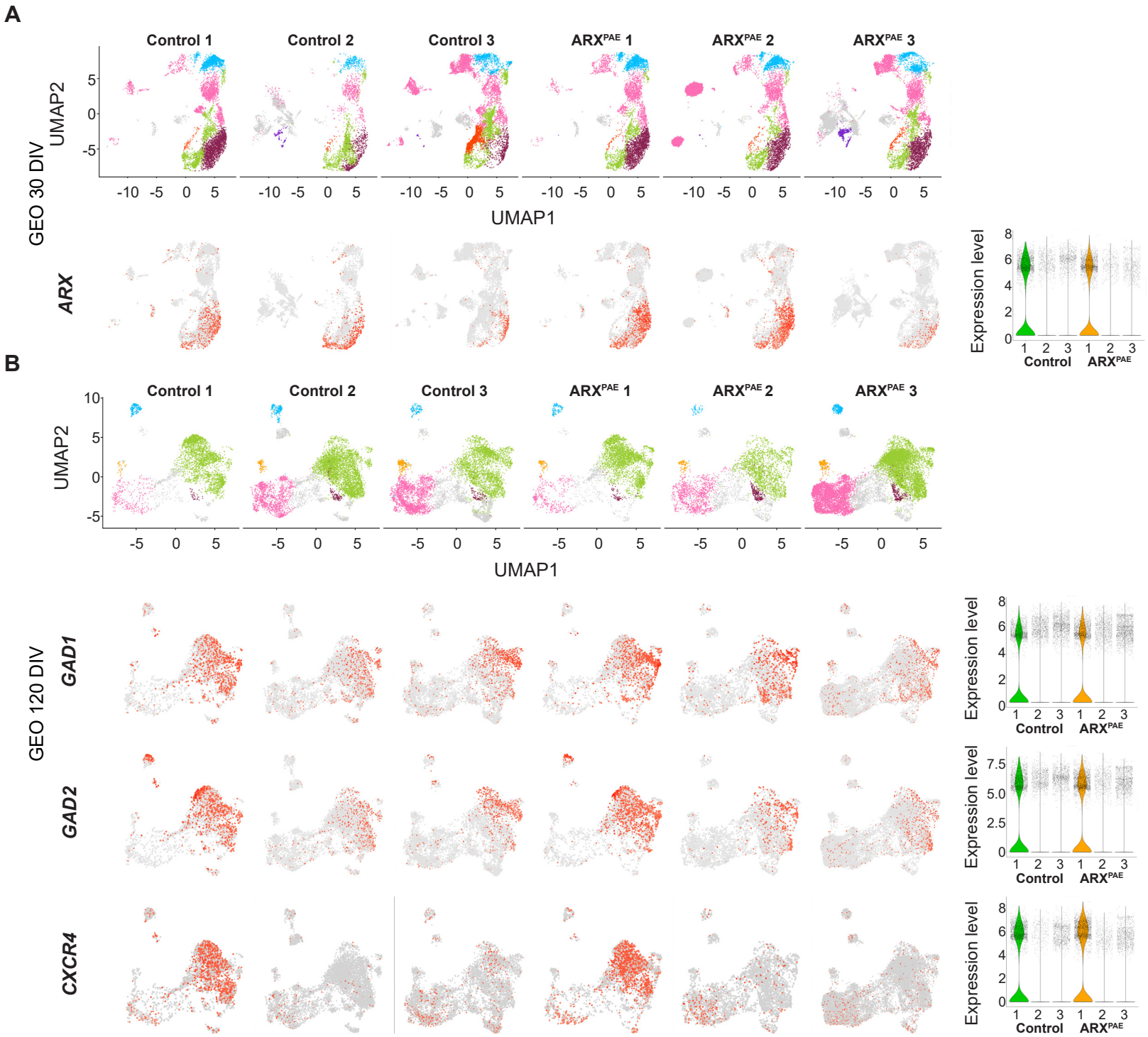
A
Control 1
Control 2
Control 3
ARX^PAE 1
ARX^PAE 2
ARX^PAE 3
GEO 30 DIV
UMAP2
UMAP1
ARX
Expression level
Control
ARX^PAE
B
GEO 120 DIV
GAD1
GAD2
CXCR4

A

Control

ARX^{PAE}

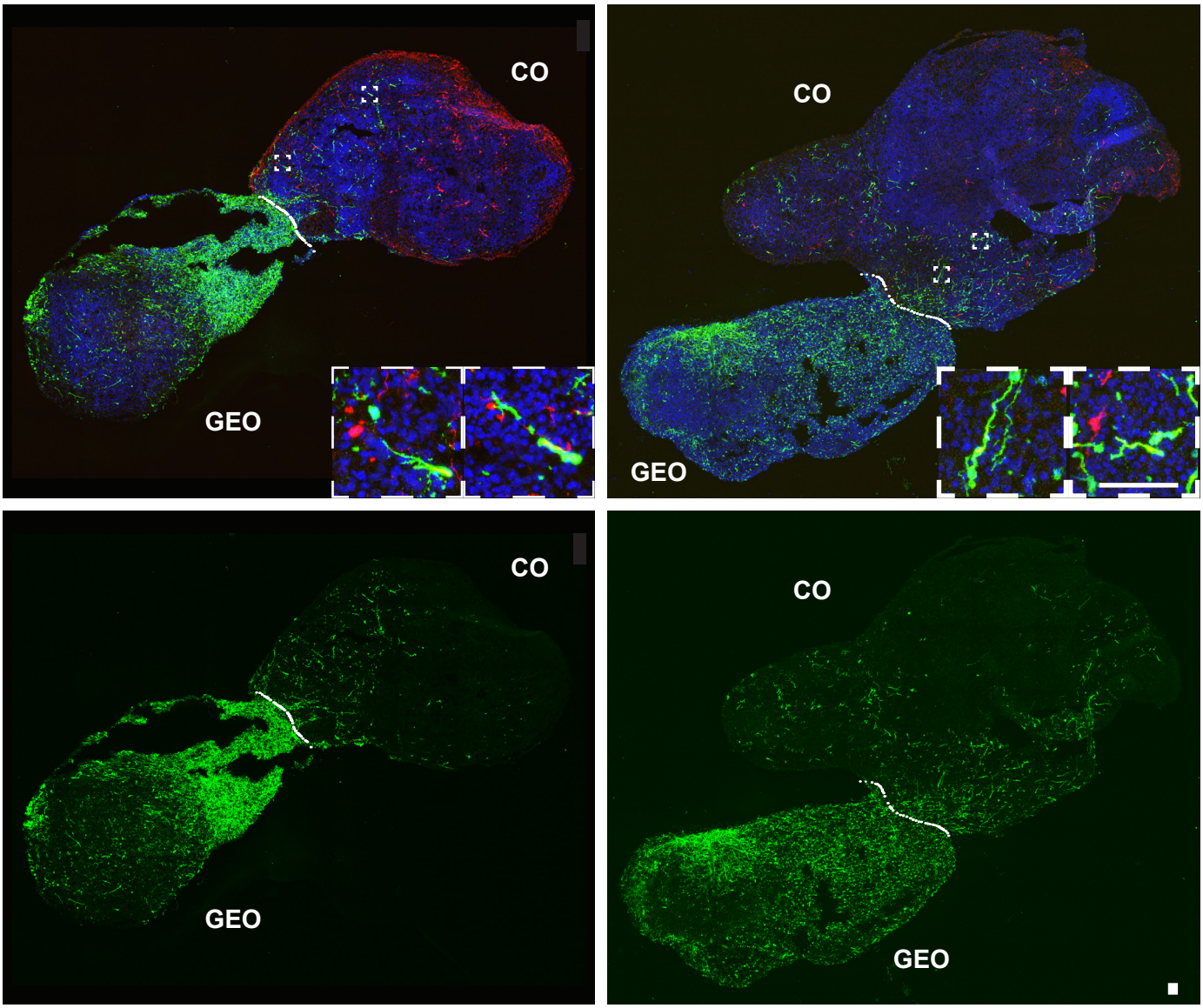

DAPI hSynapsin-mCherry hDLX1/2b:GFP

B

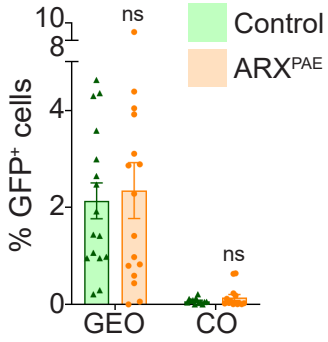

Figure S12

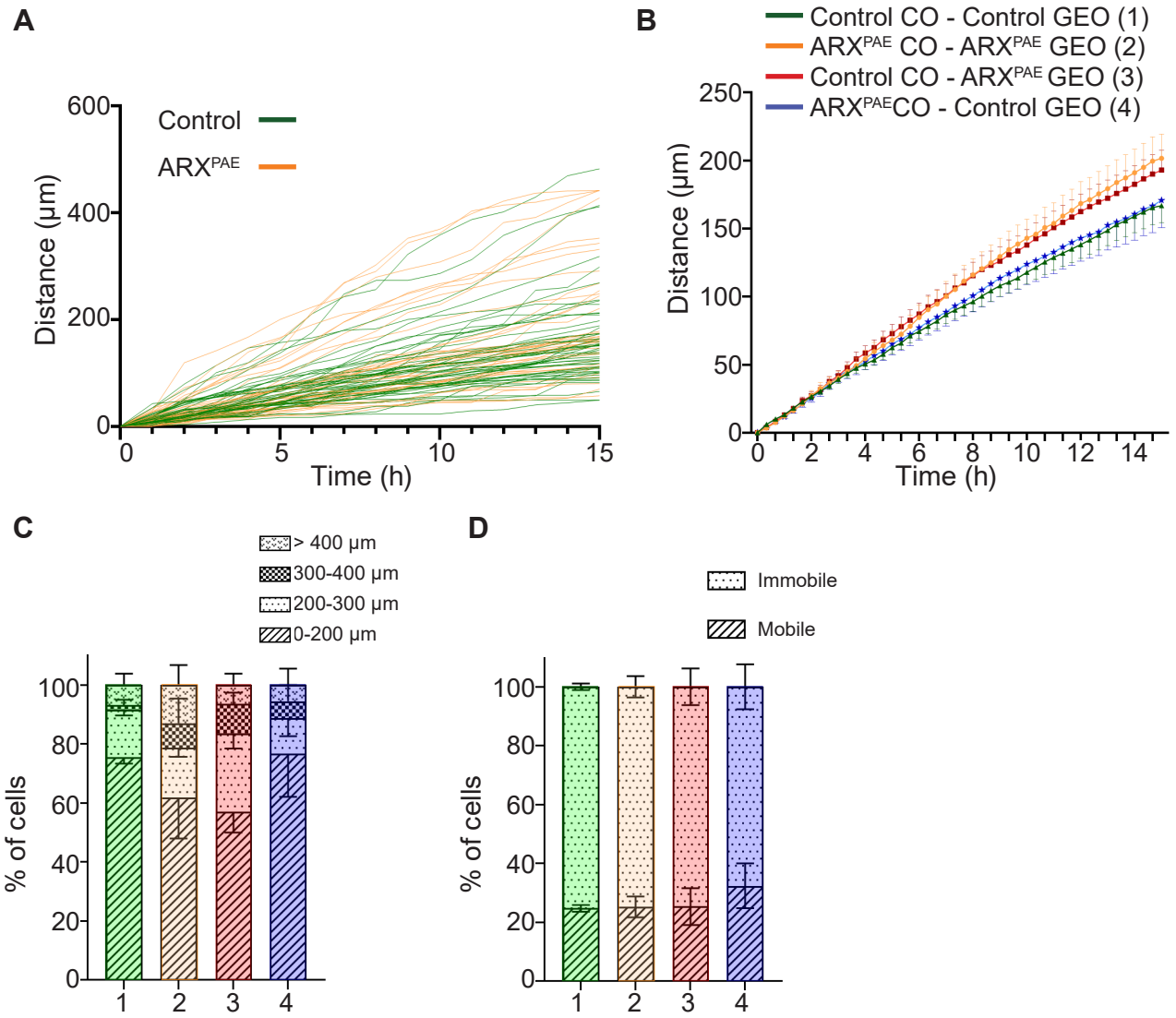
A
Control
ARXPAE
Distance (µm)
Time (h)
B
Control CO - Control GEO (1)
ARXPAE CO - ARXPAE GEO (2)
Control CO - ARXPAE GEO (3)
ARXPAECO - Control GEO (4)
Distance (µm)
Time (h)
C
> 400 µm
300-400 µm
200-300 µm
0-200 µm
% of cells
D
Immobile
Mobile
% of cells

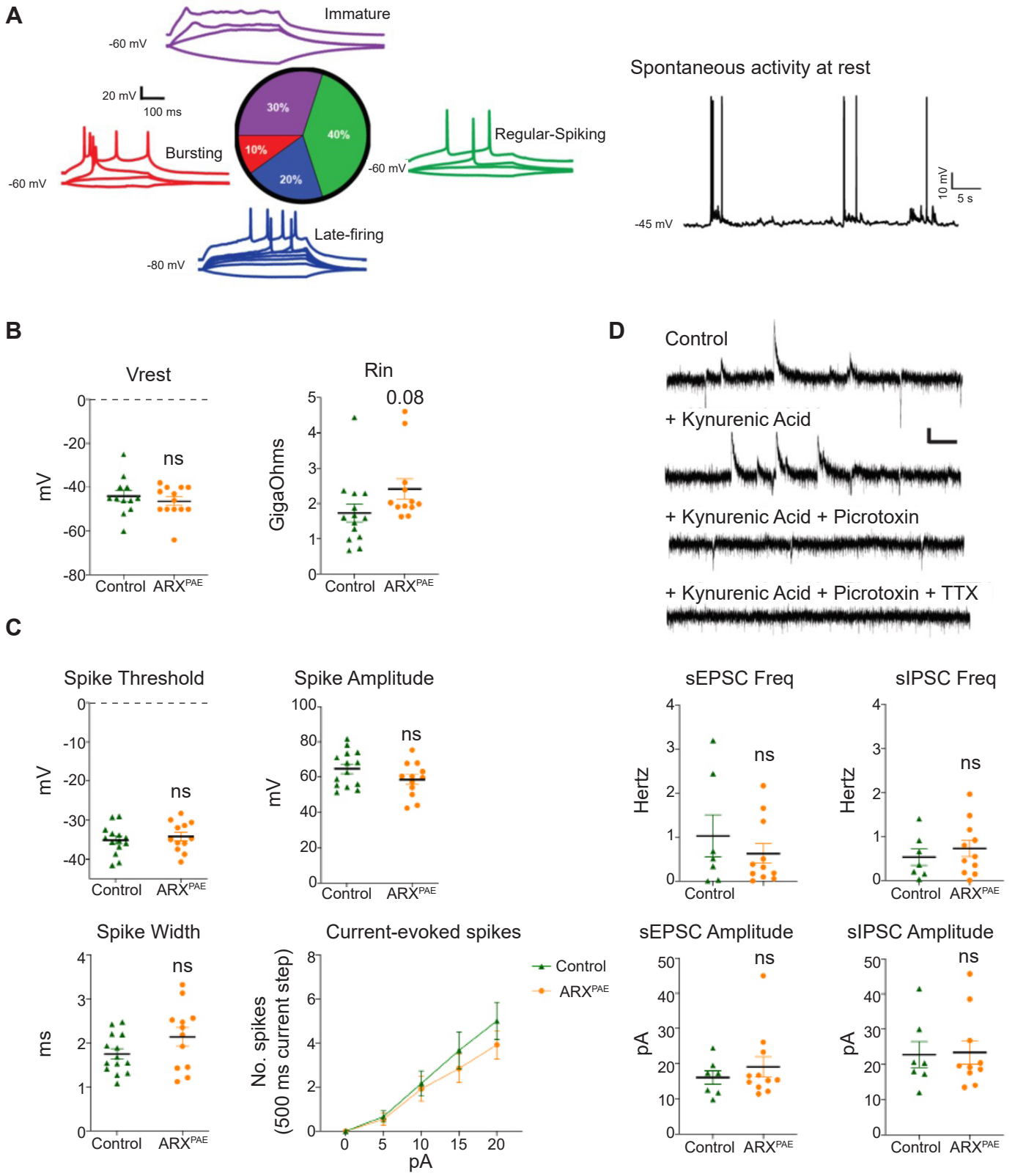
A
Immature
-60 mV
20 mV
100 ms
Bursting
-60 mV
30%
40%
10%
20%
Regular-Spiking
-60 mV
Late-firing
-80 mV
Spontaneous activity at rest
10 mV
5 s
-45 mV
B
Vrest
mV
ns
Control
ARXPAE
Rin
0.08
GigaOhms
Control
ARXPAE
D
Control
+ Kynurenic Acid
+ Kynurenic Acid + Picrotoxin
+ Kynurenic Acid + Picrotoxin + TTX
C
Spike Threshold
mV
ns
Control
ARXPAE
Spike Amplitude
mV
ns
Control
ARXPAE
sEPSC Freq
Hertz
ns
Control
sIPSC Freq
Hertz
ns
Control
ARXPAE
Spike Width
ms
ns
Control
ARXPAE
Current-evoked spikes
No. spikes
(500 ms current step)
pA
Control
ARXPAE
sEPSC Amplitude
pA
ns
Control
ARXPAE
sIPSC Amplitude
pA
ns
Control
ARXPAE